Order and disorder in two- and three-dimensional Bénard convection

By JAMES H. CURRY,

University of Colorado, Boulder, CO 80309

JACKSON R. HERRING,

National Center for Atmospheric Research, Boulder, CO 80303

JOSIP LONCARIC† AND STEVEN A. ORSZAG‡

Massachusetts Institute of Technology, Cambridge, MA 02139

The character of transition from laminar to chaotic Rayleigh–Bénard convection in a fluid layer bounded by free-slip walls is studied numerically in two and three space dimensions. While the behaviour of finite-mode, limited-spatial-resolution dynamical systems may indicate the existence of two-dimensional chaotic solutions, we find that, this chaos is a product of inadequate spatial resolution. It is shown that as the order of a finite-mode model increases from three (the Lorenz model) to the full Boussinesq system, the degree of chaos increases irregularly at first and then abruptly decreases; no strong chaos is observed with sufficiently high resolution.

In high-Prandtl-number σ two-dimensional Boussinesq convection, it is found that there are finite critical Rayleigh numbers Ra for the onset of single- and two-frequency oscillatory motion, $Ra \gtrsim 60Ra_c$ and $Ra \gtrsim 290Ra_c$ respectively, for $\sigma = 6.8$. These critical Rayleigh numbers are much higher than those at which three-dimensional convection achieves multifrequency oscillatory states. However, in two dimensions no additional complicating fluctuations are found, and the system seems to revert to periodic, single-frequency convection at high Rayleigh number, e.g. when $Ra \gtrsim 800Ra_c$ at $\sigma = 6.8$.

In three dimensions with $\sigma = 10$ and aspect ratio $1/\sqrt{2}$, single-frequency convection begins at $Ra \approx 40Ra_c$ and two-frequency convection starts at $Ra \approx 50Ra_c$. The onset of chaos seems coincident with the appearance of a third discrete frequency when $Ra \gtrsim 65Ra_c$. This three-dimensional transition process may be consistent with the scenario of Ruelle, Takens & Newhouse (1978).

As Ra increases through the chaotic regime, various measures of chaos show an increasing degree of small-scale structure, horizontal mixing and other characteristics of thermal turbulence. While the three-dimensional energy in these flows is still quite small, it is evidently sufficient to overcome the strong dynamical constraints imposed by two dimensions.

Gollub & Benson (1980) found experimentally that frequency modulation of lower boundary temperature $Ra(t) = Ra(0)[1 + \epsilon \sin \omega t]$ induces chaotic behaviour in a quasi-periodic flow close to transition. We investigate numerically the effects of finite modulation of Ra on the flow far below natural transition ($R = 50Ra_c$). By choosing $\epsilon = 0.1$ and the Rayleigh-number oscillation frequency ω incommensurate with the

---

† Present address: Pierce Hall, Harvard University, Cambridge, MA 02138.

‡ Present address: Princeton University, Princeton, NJ 08544.

frequencies of the quasi-periodic motion, transition to chaos is induced early. This result also seems consistent with the Ruelle *et al.* scenario and leads to the conjecture that periodic modulation of the Rayleigh number of the above form in a two-frequency flow may provide the third frequency necessary for chaotic flow.

For moderate Prandtl number, $\sigma = 1$, our results show that two-dimensional flow seems free of oscillation, while three-dimensional flow is vigorously turbulent for $Ra \gtrsim 70 Ra_c$.

1. Introduction

Recent mathematical work on dynamical systems has suggested several ways that chaotic behaviour can develop. Ruelle, Takens & Newhouse (1978) suggest a scenario in which chaos is likely to be obtained as a parameter (like the Rayleigh number), that describes an effective driving force in a physical system, changes. Typically, there is a range of parameter values in which the system has only a stable attracting stationary solution. As the parameter increases beyond some critical value, there may be a transfer of stability from the stationary solution to a limit cycle (possibly through a Hopf bifurcation). As the parameter changes further in this scenario the periodic solution transfers its stability to a quasiperiodic solution having two incommensurate frequencies. Changing the parameter further causes the two-dimensional torus on which the motion was quasi-periodic to become unstable, possibly being replaced with motion on a three-dimensional torus or being attracted to a chaotic solution which exhibits broadband spectral excitation (possibly superimposed on a discrete spectrum).

The Ruelle–Takens–Newhouse transition scenario should be contrasted with that proposed by Landau (Landau & Lifschitz 1959). Landau suggested that broadband turbulent excitations are only achieved after an infinite number of bifurcations through which the system achieves successively more complicated quasiperiodic states. In contrast, the Ruelle–Takens–Newhouse scheme suggests that chaos is achieved after only three incommensurate frequencies have been encountered. Other scenarios for transition to chaos are the 'universal' routes via period doubling (Feigenbaum 1978) or quasiperiodic states (Rand *et al.* 1982) and intermittent generation of chaos (Pomeau & Manneville 1980).

In a convecting fluid layer with fixed physical properties, the forcing parameter is conveniently chosen to be the Rayleigh number, denoted Ra and defined for the units used in this paper in (2.9). The Rayleigh number is a non-dimensional measure of the buoyancy force due to the heated bottom wall driving the convection. In order to determine how well Rayleigh–Bénard convection fits the classification scheme described above, it is convenient to define five values of the Rayleigh number that distinguish various flow regimes. *In any given system, some or all of these Rayleigh numbers may be nonexistent.* First, the linear critical Rayleigh number Ra_c is defined so that the heat-conducting motionless state of the fluid is stable to infinitesimal disturbances for $Ra < Ra_c$ and is unstable for $Ra > Ra_c$. As Ra increases beyond Ra_c steady-state convecting rolls appear. These rolls are two-dimensional in character. Next, Ra_1 is defined as that Rayleigh number at which these rolls undergo a bifurcation to a periodic, possibly three-dimensional, oscillatory state. Periodic convection ensues as Ra increases above Ra_1. At Ra_2 a second (normally incommensurate) frequency appears, so the flow is quasi-periodic. If the second frequency is commensurate with the first, phase locking occurs so the flow is still periodic but with

a new frequency. Then at Ra_t the flow undergoes transition to a chaotic state with broadband frequency response. Of course there may also be transitional numbers Ra_n for $n \geqslant 3$ in which n distinct incommensurate frequencies are observable; the Ruelle *et al.* scenario suggests that 'typical' systems should satisfy $Ra_t = Ra_3$. Finally there is another critical Rayleigh number that it is useful to define although its existence is not anticipated by the generic mathematical analysis outlined above. The Rayleigh number Ra_1' is defined as that value of Ra at which a reverse transition from quasi-periodic or chaotic flow to periodic flow occurs as Ra increases. While the flow just below Ra_1' has at least two incommensurate frequencies present, that just above Ra_1' has but one significant frequency. Furthermore, there may even be bands of Rayleigh number between Ra_t and Ra_1' in which the flow reverts to quasi-periodic behaviour. Finally we emphasize once again that some or all of these putative critical Ra may not exist in any particular realization of a real flow.

In addition to the recent developments in the mathematical theory of dynamical systems, there have also been several studies of specific low-order systems of ordinary differential equations, often obtained by Galerkin approximation to the Boussinesq equations for free-slip Rayleigh–Bénard convection. In his seminal paper Lorenz (1963) studied the three-component dynamical system obtained by Galerkin projection of the equations of two-dimensional convection in the box $0 \leqslant x \leqslant \pi \sqrt{2}, \ 0 \leqslant z \leqslant \pi$ on solutions of the form

$$\left. \begin{aligned} \psi &= a(t) \sin \frac{x}{\sqrt{2}} \sin z, \\ T &= b(t) \cos \frac{x}{\sqrt{2}} \sin z + c(t) \sin 2z. \end{aligned} \right\} \tag{1.1}$$

where ψ is the stream function and T is the deviation of the temperature from the conduction profile $-z$. The result is Lorenz's model equations

$$\left. \begin{aligned} \dot{a} &= -\sigma a + \sigma b, \\ \dot{b} &= -ac + ra - b, \\ \dot{c} &= ab - \tfrac{8}{3}c, \end{aligned} \right\} \tag{1.2}$$

where $r = Ra/Ra_c$ and σ is the Prandtl number (see (2.10)). (Here a, b, c are proportional to a_{11}, b_{11}, b_{02} respectively in the generalized expansion (2.14)–(2.15).)

Lorenz's model gives Ra_c exactly; at $r = 1$ the conductive state $a = b = c = 0$ becomes unstable. The steady convective state is stable for all $Ra > Ra_c$ unless $\sigma > \tfrac{11}{3}$.

Some specific results for $\sigma = 10$ illuminate the kinds of solutions that are obtained for moderately large σ. No critical numbers Ra_1 or Ra_2 are observed, but it is found that chaos starts abruptly at $Ra_t \approx 24.74 Ra_c$. On the other hand, chaos disappears just as abruptly for $Ra_1' \approx 320 Ra_c$; for $Ra_t < Ra < Ra_1'$ there are many intervals of Ra in which the flow is chaotic. For $Ra > Ra_1'$ the flow is periodic. For certain parameter ranges, this behaviour of the system fits the Pomeau–Manneville scenario and also exhibits period doublings.

An extension of the Lorenz model was considered by Curry (1978, 1979) in which the two-dimensional Boussinesq equations are projected on a 14-variable subspace. In Curry's model with $\sigma = 10$ the sequence of bifurcations leading to chaos is as follows. For $r < 1$ the conductive state is stable. For $r > 1$ there is a bifurcation to convection. The steady convective solutions remain stable until $r = 43.50$, where a Hopf bifurcation occurs. The resulting periodic orbit remains stable until $r = 44.40$, where a single period-doubling bifurcation occurs. When r exceeds 44.85 the resulting

period-doubled orbit undergoes a bifurcation to a two-dimensional torus. As the parameter value increases further, the motion on the torus first becomes phase-locked and then becomes quasi-periodic with two incommensurate frequencies. Then at $r = 45.18$ chaos is observed. Thus the sequence of bifurcations for Curry's 14-variable model seems to be consistent with the Ruelle–Takens–Newhouse scenario.

In this paper we extend these earlier studies of the behaviour of systems of ordinary differential equations to study the behavior of free-slip Rayleigh–Bénard convection. Specifically our objectives are twofold. First we examine the resemblance of the behaviour of low-order dynamical systems to the behaviour of a Boussinesq fluid. Secondly we study in some detail the nature of transitions and turbulence in two-and three-dimensional Boussinesq fluids. In §2 we summarize the dynamical equations and numerical methods used in our studies. Then in §3 we compare the transitional behaviour of finite-mode systems obtained by Galerkin projection of the two-dimensional dynamics to accurate solutions of the Boussinesq equations. In §4 the states of high Prandtl number two-dimensional convection are studied. Then in §5 the character of three-dimensional convection is discussed.

2. Formulation and numerical solution

The equations of motion of a Boussinesq fluid layer are

$$\frac{\partial \boldsymbol{v}}{\partial t} = \boldsymbol{v} \times \boldsymbol{\omega} - \boldsymbol{\nabla}(p + \tfrac{1}{2}v^2) + \alpha T \hat{\boldsymbol{z}} + \nu \nabla^2 \boldsymbol{v}, \tag{2.1}$$

$$\frac{\partial T}{\partial t} + \boldsymbol{v} \cdot \boldsymbol{\nabla} T = \beta w + \kappa \nabla^2 T, \tag{2.2}$$

$$\boldsymbol{\nabla} \cdot \boldsymbol{v} = 0. \tag{2.3}$$

Here $\boldsymbol{v} = (u, v, w)$ is the velocity field at $\boldsymbol{x} = (x, y, z)$, $\boldsymbol{\omega} = \boldsymbol{\nabla} \times \boldsymbol{v}$ is the vorticity, p is the pressure (assuming the density to be normalized to 1), T is the deviation of the temperature from the conduction profile $-\beta z$ (so that $T - \beta z$ is the actual temperature), ν is the kinematic viscosity, κ is the thermal conductivity, and α is the thermal expansion coefficient (in units where the gravitational acceleration and the density are 1). The flow is assumed to occur in the region

$$0 \leqslant x \leqslant \lambda H, \quad 0 \leqslant y \leqslant \mu H, \quad 0 \leqslant z \leqslant H. \tag{2.4}$$

Periodic boundary conditions are applied in x and y with periods λH and μH respectively:
$$\boldsymbol{v}(x + m\lambda H, y + n\mu H, z, t) = \boldsymbol{v}(x, y, z, t)$$

for all integers m, n. Free-slip (no-stress) impermeable boundary conditions are applied at $z = 0, H$, so

$$\frac{\partial u}{\partial z} = \frac{\partial v}{\partial z} = w = 0 \quad (z = 0, H), \tag{2.5}$$

while T is assumed to satisfy the conducting-boundary condition

$$T = 0 \quad (z = 0, H). \tag{2.6}$$

Also, $\beta > 0$ corresponds to a thermally unstable layer, while $\beta < 0$ gives a thermally stable layer.

Equations (2.1)–(2.6) may be non-dimensionalized in terms of the vertical thermal

diffusion time H^2/κ, the vertical lengthscale H, the velocity scale κ/H and the temperature scale $|\beta| H$. In these units (2.1) and (2.2) become

$$\frac{\partial \boldsymbol{v}}{\partial t} = \boldsymbol{v} \times \boldsymbol{\omega} - \boldsymbol{\nabla}(p + \tfrac{1}{2}v^2) + Ra\,\sigma T\boldsymbol{z} + \sigma \nabla^2 \boldsymbol{v}, \tag{2.7}$$

$$\frac{\partial T}{\partial t} + \boldsymbol{v} \cdot \boldsymbol{\nabla} T = (\text{sgn }\beta)\, w + \nabla^2 T, \tag{2.8}$$

where
$$Ra = \frac{\alpha |\beta| H^4}{\nu \kappa}, \tag{2.9}$$

$$\sigma = \nu/\kappa \tag{2.10}$$

are respectively the Rayleigh and Prandtl numbers. With this non-dimensionalization, the critical Rayleigh number for onset of convection in the layer $0 \leqslant z \leqslant 1$ is $Ra_c = \frac{27}{4}\pi^4 \approx 657$, which is achieved for $\lambda^2 + \mu^2 = 2\pi$, independent of σ, provided that $\beta > 0$.

Equations (2.1)–(2.6) are solved using spectral methods (Orszag 1971). The dependent flow variables are expanded in the Fourier series

$$\begin{Bmatrix} u \\ v \\ w \\ T \end{Bmatrix} (x,y,z,t) = \sum_{|m| \leqslant \frac{1}{2}M} \sum_{|n| \leqslant \frac{1}{2}N} \sum_{p=0}^{P} \begin{Bmatrix} \hat{u} \\ \hat{v} \\ \hat{w} \\ \hat{T} \end{Bmatrix} (m,n,p,t)\, e^{2\pi i(mx/\lambda + ny/\mu)} \begin{Bmatrix} \cos \pi pz \\ \cos \pi pz \\ \sin \pi pz \\ \sin \pi pz \end{Bmatrix}. \tag{2.11}$$

The nonlinear terms are evaluated by fast-transform methods with aliasing terms usually removed. Time-stepping is done by a leapfrog scheme for the nonlinear terms and an implicit scheme for the viscous terms (either the Crank–Nicolson or backwards Euler scheme, depending on application). The pressure term is computed in Fourier representation by local algebraic manipulation of the incompressibility constraint (2.3).

The above method has been implemented for both two and three space dimensions. In the two-dimensional code ($N = 0$ in (2.11)) typical computer times on the Cray-1 computer are about 0.15 s per time step with $M = P = 128$; this time scales as $MP \log_2 MP$. The three-dimensional code on the Cray-1 computer requires 0.6 s per time step with $M = N = P = 32$; this time scales as $MNP \log_2 MNP$. Typical runs reported below involve as many as 8×10^4 time steps; typical results are obtained using $M = 64, P = 32$ in two dimensions and $M = N = 32, P = 16$ in three dimensions, and involve less than 2 h of computer time per run in three dimensions.

In order to increase the effective spatial resolution of small scales in the flows without increasing substantially the computational expense, it is useful to study flows satisfying certain symmetry properties. It may be shown that (2.1)–(2.6) are consistent with the following symmetries of the Fourier components in (2.11) (written for the two-dimensional case only):

$$\left.\begin{aligned} \hat{u}(m,p,t) &= -\hat{u}(-m,p,t), \\ \hat{w}(m,p,t) &= \hat{w}(-m,p,t), \\ \hat{T}(m,p,t) &= \hat{T}(-m,p,t). \end{aligned}\right\} \tag{2.12}$$

and
$$\hat{u} = \hat{w} = \hat{T} = 0 \quad \text{unless} \quad m + p \equiv 0 \,(\text{mod } 2). \tag{2.13}$$

Equations (2.12) and (2.13) reduce the required storage and work per time step by about a factor 4. The technical details of how to do this are described in appendices

B and C of Brachet *et al.* (1983). With the symmetries (2.12) and (2.13), the two-dimensional code with $M = P = 128$ requires about 0.04 s per time step on the Cray-1. Results are reported here using the symmetrized code for two-dimensional simulations only.

With the symmetries (2.12) and (2.13) the two-dimensional stream function and temperature field may be expanded as

$$\psi(x, z, t) = \sum_{\substack{m+p \text{ even} \\ 1 \leqslant m \leqslant \overline{M} \\ 1 \leqslant p \leqslant P}} a_{mp}(t) \sin \frac{2m\pi x}{\lambda} \sin p\pi z, \tag{2.14}$$

$$T(x, z, t) = \sum_{\substack{m+p \text{ even} \\ 1 \leqslant m \leqslant \overline{M} \\ 1 \leqslant p \leqslant P}} b_{mp}(t) \cos \frac{2m\pi x}{\lambda} \sin p\pi z, \tag{2.15}$$

where the stream function ψ is related to the velocity field by $u = \partial\psi/\partial z, w = -\partial\psi/\partial x$. Note that (2.14) and (2.15) are special forms of (2.11) with $\overline{M} = \frac{1}{2}M$.

3. Spurious chaos of truncated dynamical systems

In this section we investigate how well the behaviour of low-order systems of ordinary differential equations reflects that of the partial differential equations governing a convecting layer. The problem is that, while it may be justified to use only a few degrees of freedom to represent the steadily convecting flow states achieved when Ra just exceeds Ra_c, it is not apparent that such truncated flow representations are valid for the more complicated flow states that may be obtained at higher Ra.

It has been noticed previously by us (see Orszag & Kells 1980; also Marcus 1981; Treve & Manley 1982) that too little spatial resolution in the solution of partial differential equations can induce chaos in the computed solution which disappears when adequate resolution is used. This effect may perhaps be considered surprising as one might expect that, as partial differential equations involve an infinite number of degrees of freedom, their solutions would be richer and more chaotic than solutions to finite-mode dynamical systems. On the contrary, the sea of weakly excited small-scale modes in a dissipative dynamical field seems to act as an effective damping, or eddy viscosity, which tends to reduce the tendency of modes to exchange energy in a chaotic way.

Here we show that high-Prandtl-number Rayleigh–Bénard convection also exhibits spurious chaos when inadequate resolution is used. In fact, while the hierarchy of models that generalize the low-order systems of Lorenz (1963) and Curry (1979) apparently do each exhibit some degree of randomness for high σ, the full two-dimensional Boussinesq equations, used to generate these finite-mode models, seem to have solutions that are never chaotic (or, at least, not strongly chaotic) to the resolution and accuracy of our computations. The apparent absence of true chaos in high-Prandtl-number two-dimensional convection will be discussed in §4.

To illustrate spurious chaos at low spatial resolution, we consider the solution to the system (2.7), (2.8), (2.12)–(2.15) with $\sigma = 20$, $Ra = 120Ra_c$. In figure 1 we plot, for various $\overline{M}$ and P in (2.14) and (2.15), time histories of the temperature Fourier coefficient $b_{02}(t)$ and its power-spectral density $|\tilde{b}_{02}(f)|^2$ computed as

$$\tilde{b}_{02}(f) = \frac{1}{\overline{t}} \int_0^{\overline{t}} (b_{02} - \overline{b}_{02}) \left(1 - \cos \frac{2\pi t}{\overline{t}}\right) e^{-i2\pi ft} \, dt + \overline{b}_{02} \delta_{f0}, \tag{3.1}$$
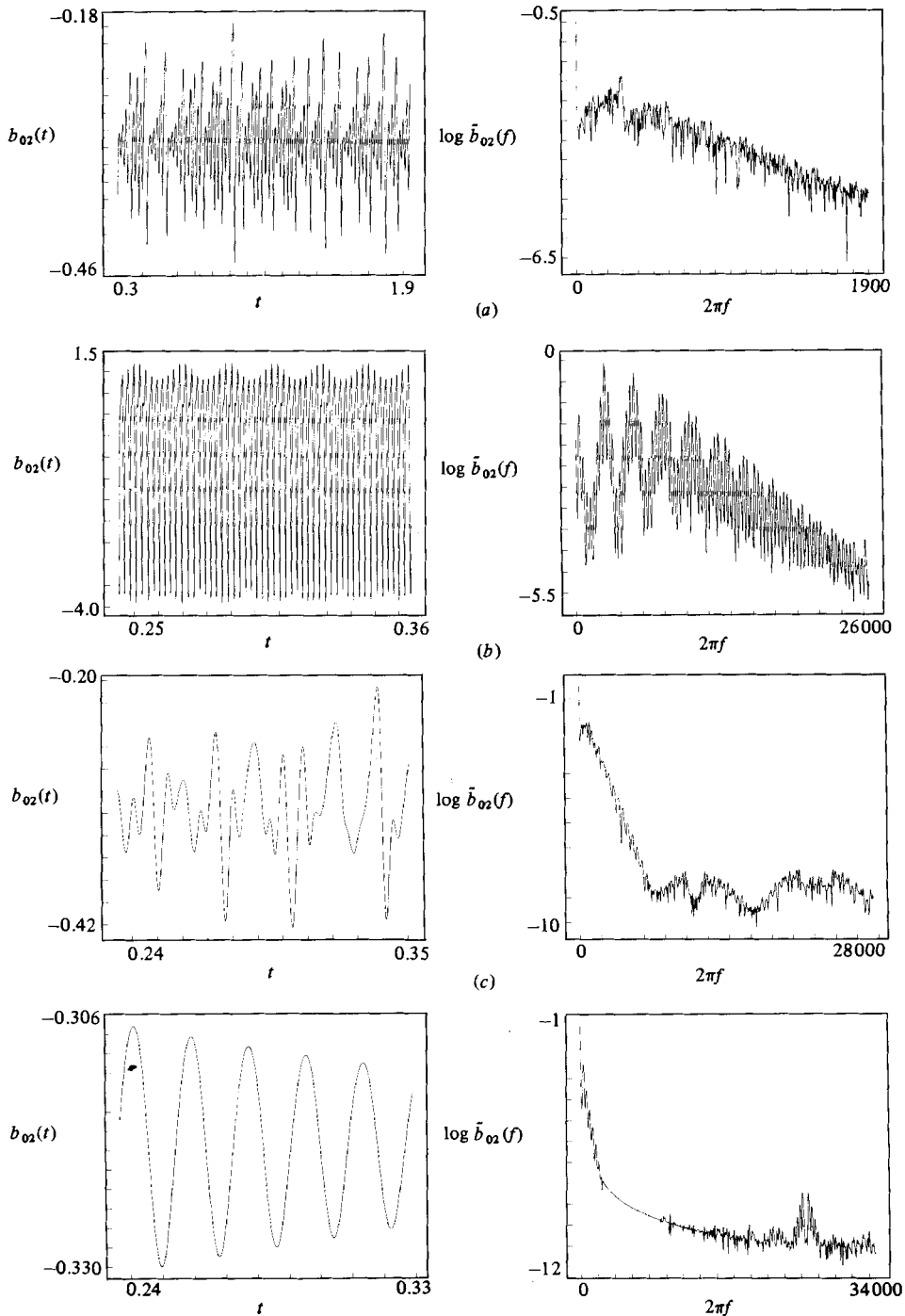
FIGURE 1. Time series $b_{02}(t)$ and time spectra $\log \bar{b}_{02}(f)$ for two-dimensional truncated symmetric convection runs at $Ra = 120Ra_c$, $\sigma = 20$, $\lambda = 2\sqrt{2}$ for various $\overline{M}, P$: (a) $\overline{M} = 1$, $P = 2$; (b) 2, 3; (c) 3, 4; (d) 5, 6. The initial conditions are $a_{11} = 1$ with all other Fourier components zero. Notice that the qualitative behaviour of the time series and spectral changes markedly with changing modal truncation.
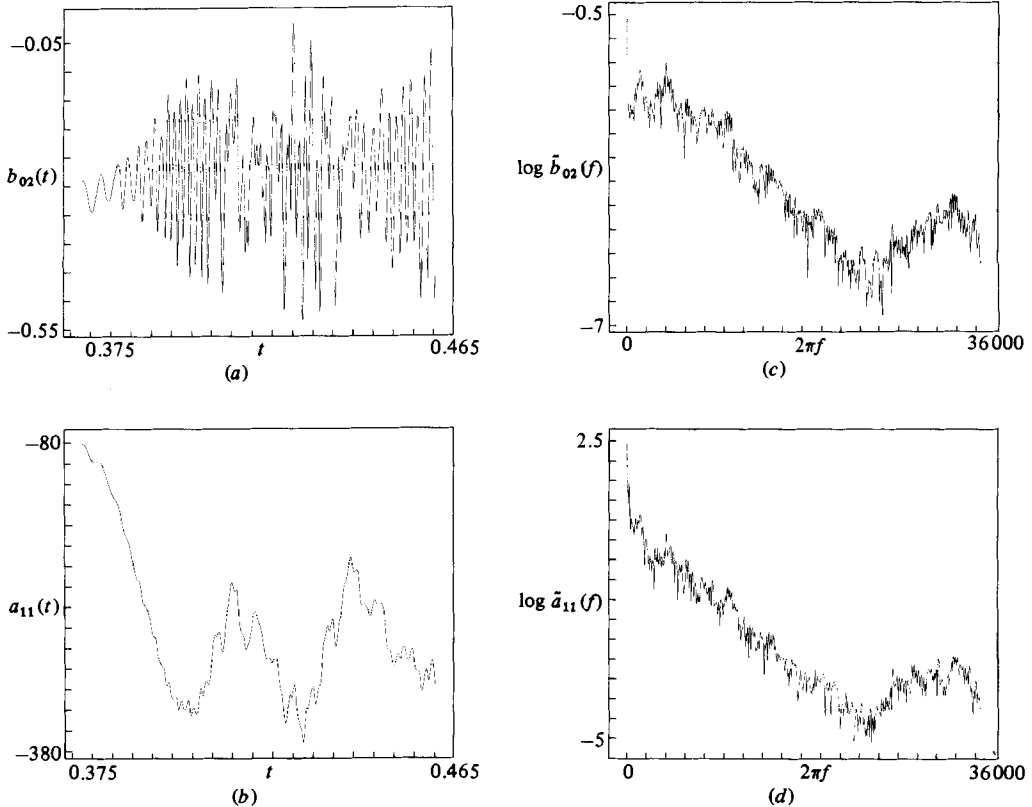
FIGURE 2. Time series (a) $b_{02}(t)$ and (b) $a_{11}(t)$, and time spectra (c) $\log \tilde{b}_{02}(f)$ and (d) $\log \tilde{a}_{11}(f)$, for the same run as in figure 1 but with $\bar{M} = P = 7$. Observe the strongly chaotic nature of this solution.

where $\bar{b}_{02} = \bar{t}^{-1} \int_0^t b_{02} \, dt$. The window function $1 - \cos (2\pi t/\bar{t})$ is used to reduce finite-time effects. Also, the time interval $0 \leqslant t \leqslant \bar{t}$ is shifted so that it represents roughly the final third of a long-time integration of the equations of motion. The Lorenz system ($\bar{M} = 1$, $P = 2$) has a weakly chaotic solution, as evidenced by the broadly excited spectral density. On the other hand, with $\bar{M} = 2$, $P = 3$, a quasi-periodic solution is achieved with discrete lines at $f_1 \approx 54$, $f_2 \approx 4.3 \times 10^2$. For $\bar{M} = 3$, $P = 4$ the solution is apparently chaotic again with somewhat broader spectral excitation than in the Lorenz system. The solution becomes less chaotic again at $\bar{M} = 5$, $P = 6$.

In figure 2 we plot time histories and power spectra of a_{11} and b_{02} for the case $\bar{M} = P = 7$. Here the solution is strongly chaotic, as evidenced by its spectrum. As $\bar{M}$ and P increase further, the chaos abruptly disappears. In figure 3 we plot time histories and power spectra of a_{11} and b_{02} for $\bar{M} = P = 19$ and $\bar{M} = P = 41$. With both resolutions the solutions are periodic with discrete line spectra and do not sensibly differ from each other. The agreement between the $\bar{M} = P = 19$ and $\bar{M} = P = 41$ results (and with other computations at $\bar{M} = 41$, $P = 84$ and $\bar{M} = 84$, $P = 41$) demonstrate convergence to the solution of the Boussinesq equations at $\sigma = 20$, $Ra = 120 Ra_c$.

The behaviour just described at $\sigma = 20$, $Ra = 120 Ra_c$ seems to be typical for the two-dimensional Boussinesq problem. As $\bar{M}$ and P increase in (2.14) and (2.15), solutions at first tend to have increased complexity (though not monotonically so with
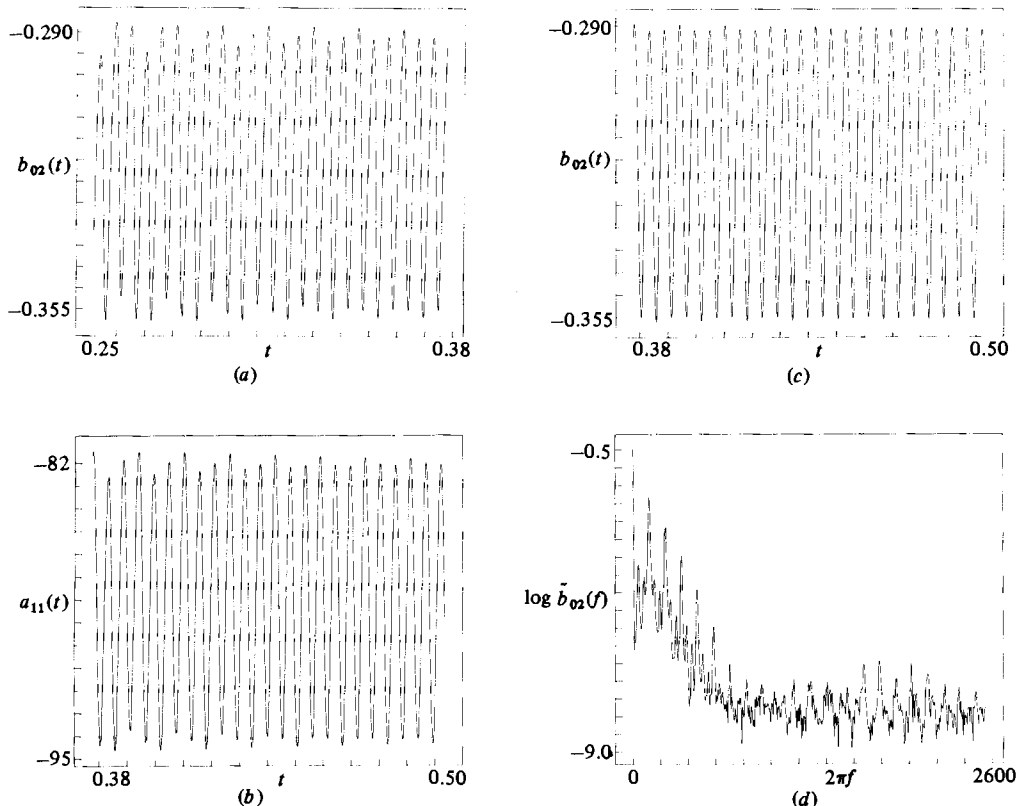
FIGURE 3. (a) Time series of b_{02} for the same run as in figures 1 and 2 but with $\overline{M} = P = 19$. (b) Time series of a_{11} for the run with $\overline{M} = P = 40$. (c) Time series of b_{02} for the run with $\overline{M} = P = 40$. (d) Time spectra $\log \tilde{b}_{02}(f)$ for the run with $\overline{M} = P = 40$. Observe that for $\overline{M} = P \gtrsim 19$ the time series is periodic and insensitive to further changes in modal truncation.

increasing $\overline{M}$ and P) and then to undergo an abrupt reverse transition into a simple periodic or at worst quasi-periodic state. Once this simple state is achieved, further increases in $\overline{M}$ and P do not affect the solution. For example, in figure 4 we plot the time series for the temperature Fourier mode b_{02} when $\sigma = 1$, $Ra = 80Ra_c$ for various low-order truncations. With sufficient resolution a stable steadily convecting state is obtained.

It is possible to recognize spurious chaos without fully checking solutions as a function of the resolution $\overline{M}$ and P. It seems that solutions exhibiting spurious chaos have large excitations in modes near the wavenumber cutoffs $\overline{M}$ and P. In figure 5 we plot the spatial spectra of kinetic and thermal energy for the runs at $\sigma = 20$, $Ra = 120Ra_c$ with $\overline{M} = P = 7, 19, 41$. The spuriously chaotic solution at $\overline{M} = P = 7$ intermittently in time has very significant excitations near the cutoff whereas the flows for $\overline{M} = P = 19, 41$ have well-defined dissipation ranges. (If, at some resolution, a temporally periodic flow is obtained it is unlikely that further increases in resolution will change its qualitative character. Indeed, smooth periodic solutions typically have well-defined (spatial) dissipation ranges in which increasing the spatial resolution gives only exponentially small corrections.)

The results of this section show that one must be very careful in inferring behaviour of physical systems from low-order dynamical models. Such models often give good
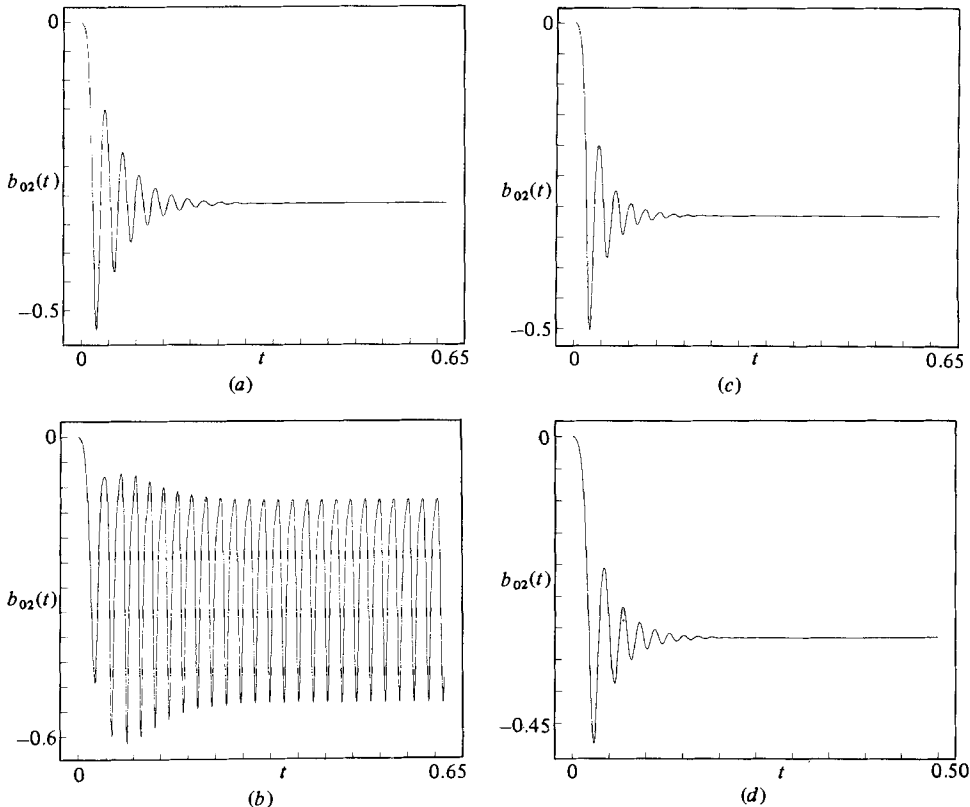
FIGURE 4. Time series of b_{02} for symmetric convection runs at $Ra = 80Ra_c$, $\sigma = 1$, $\lambda = 2\sqrt{2}$. (a) $\overline{M} = 1, P = 2$; (b) 2, 3; (c) 3, 4; (d) 19, 19. For sufficiently high modal truncation a time-asymptotic steady state is achieved.

representations of solutions that vary slowly in space, but they may misrepresent solutions whose dynamics are governed through boundary and/or internal layers beyond the resolution of the retained modes.

4. Two-dimensional time-dependent convection at $\sigma = 6.8$

In this section we consider the behaviour of two-dimensional Boussinesq convection for water ($\sigma = 6.8$) as Ra increases beyond Ra_c. All solutions discussed here are adequately resolved in the sense of §3 as their behaviour has been checked by increasing (and decreasing) the spatial-resolution parameters M and P and the time step Δt. In addition our codes have been checked by comparison with published results of Moore & Weiss (1973). The present results extend those of Moore & Weiss to $Ra/Ra_c \approx 1000$.

As Ra increases beyond Ra_c steady convection is first achieved. The behaviour for increasing Ra depends somewhat on whether or not the symmetry conditions (2.12) and (2.13) are imposed. It seems that, as found also in the rigid-boundary convection studies by McLaughlin & Orszag (1982), the symmetry-preserving steady rolls are first unstable to a symmetry-breaking instablity that leads to an oscillatory convecting state. In figure 6 we plot the time history and power spectra of the resulting oscillatory convection at $\sigma = 6.8$, $Ra = 60Ra_c$. It seems that this flow is
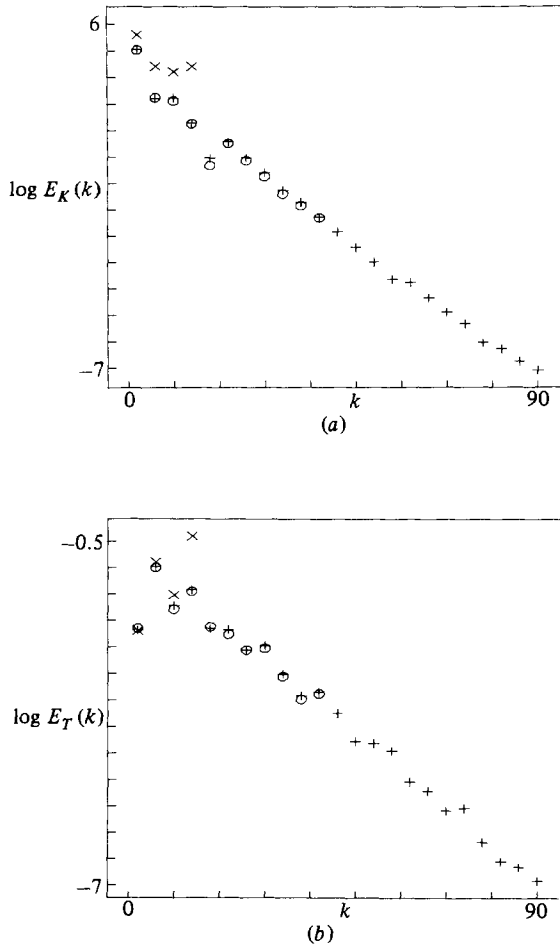
FIGURE 5. Spatial kinetic (a) and thermal (b) energy spectra for the runs plotted in figures 1–3. ×, $\overline{M} = P = 7$; ○, $\overline{M} = P = 19$; +, $\overline{M} = P = 41$. The chaotic character of the run with $\overline{M} = P = 7$ is signalled by the large energy near the spectral cutoff. Here $k^2 = (2m\pi/\lambda)^2 + (p\pi)^2$ (see (2.14) and (2.15)).

indeed periodic. Our best estimate is that there is a bifurcation of two-dimensional steady convection to two-dimensional oscillatory convection for $\sigma = 6.8$, $Ra > Ra_1 \approx 50Ra_c$.

When the symmetries (2.12) and (2.13) are forced to hold, the bifurcation to oscillatory convection is postponed to $Ra_1 \approx 90Ra_c$, consistent with the earlier results of Moore & Weiss (1973) for symmetric convection. In figure 7 time histories, spectra and mean profiles for the resulting oscillatory state $Ra = 100Ra_c$ are plotted. The flow is periodic; only harmonics of the basic energetic frequency are excited. Contour plots of temperature and streamlines at various stages through an oscillation cycle are given in figure 8. The basic oscillation period can apparently be characterized in two ways. First it is the time necessary to convect the hot and cold blobs of fluid apparent in figure 8 around the convection cell (Moore & Weiss 1973). Secondly this characteristic time seems also to be close to the Brunt–Väisälä thermal oscillation frequency based on the (stable) mean temperature gradient in the convective core of the cell (see figure 7c).
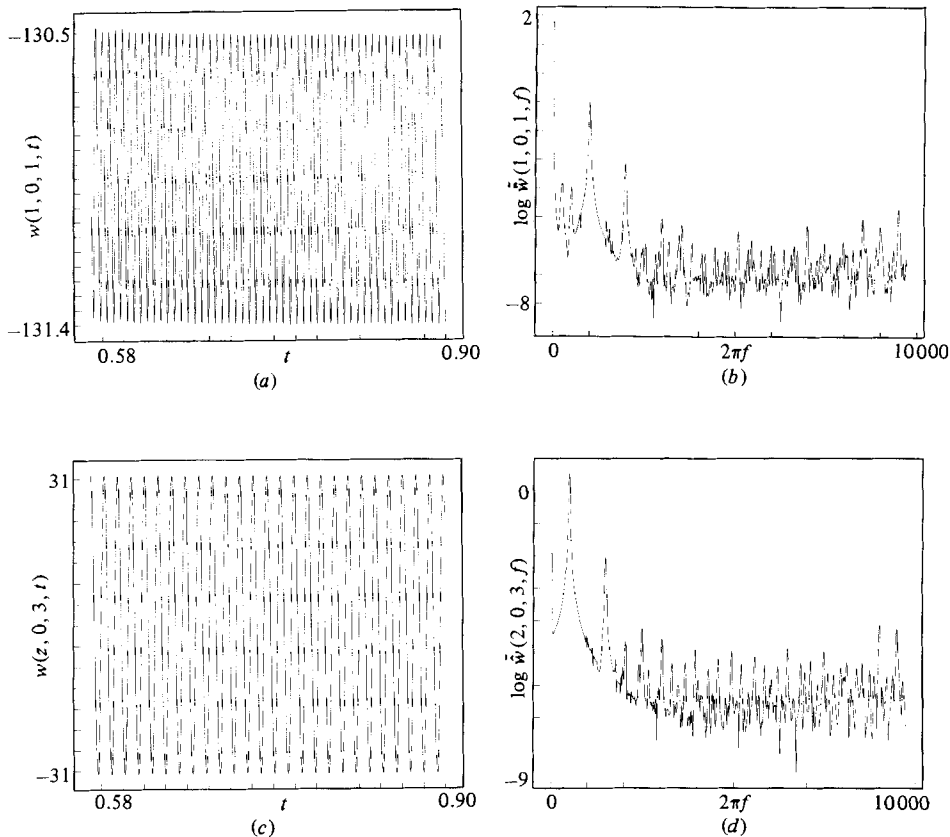
FIGURE 6. Time series and time spectra for two-dimensional non-symmetric convection at $Ra = 60Ra_\mathrm{c}$, $\sigma = 6.8$, $\lambda = 2\sqrt{2}$. (a) $\hat{w}(1,0,1,t)$ (see (2.11)); (b) $\log \hat{\bar{w}}(1,0,1,f)$; (c) $\hat{w}(2,0,3,t)$; (d) $\log \hat{\bar{w}}(2,0,3,f)$.

Because of computer limitations, our further study of transitions in two-dimensional convection is limited to the symmetric systems in which (2.12)–(2.15) hold. While we may miss some very significant phenomena because of this assumption, our results do not contradict the qualitative behaviour of check runs made without the symmetry assumptions.

For $\sigma = 6.8$ periodic convection seems to persist up to about $Ra \approx 290Ra_\mathrm{c}$. For $Ra > Ra_2 \approx 290Ra_\mathrm{c}$, a new oscillation period emerges at very low frequency. For example, in figure 9 we give time series, frequency spectra and Poincaré maps for the two-dimensional flow at $Ra = 400Ra_\mathrm{c}$. In this case, the solution is nearly periodic with a period 40 times longer than that of the most-energetic frequency component. The time-series plots given in figures 9(a, c) are over just one of these long periods; the spectra (figures 9b, d) are computed over six of these long periods. The distinct line spectrum is apparent; the separation between the lines is the low frequency of the new period.

The type of oscillatory state observed in figures 9(a, c) is remarkably similar to nearly two-dimensional flow states recently observed by Libchaber and his coworkers (private communication 1982) in low-Prandtl-number convection in a strong magnetic field (see figure 9e). Apparently the magnetic field can suppress the three-dimensional flow at low-to-moderate Ra so that the flow mimics two-dimensional behaviour; at
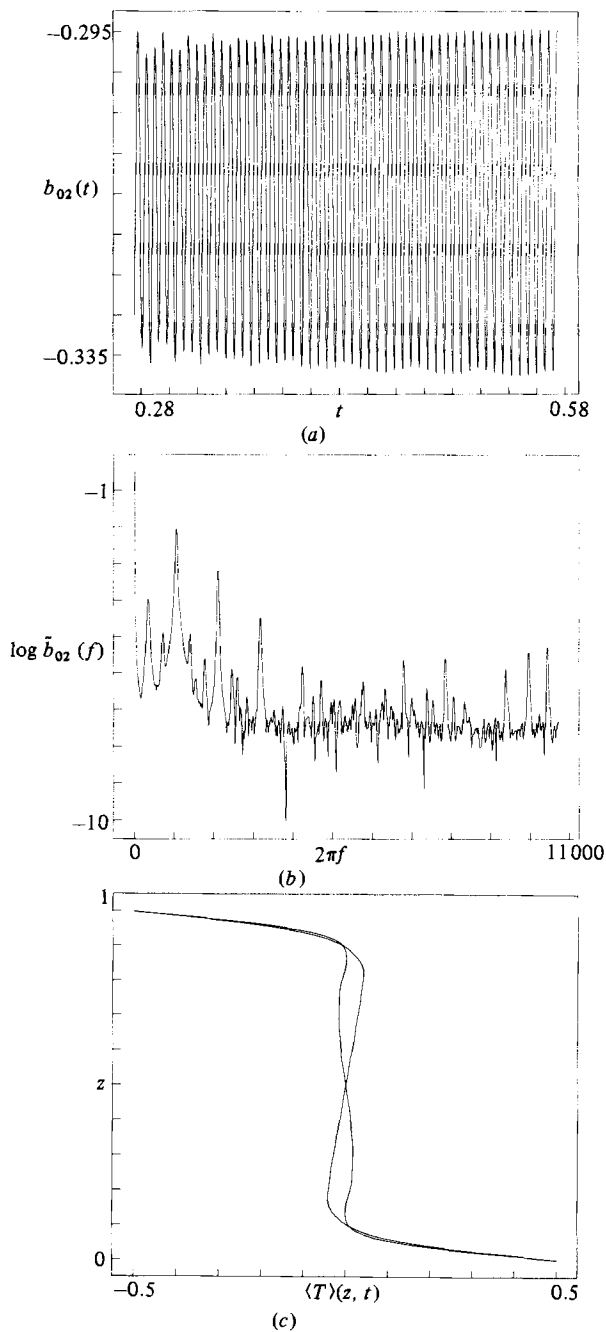
FIGURE 7. (a) Time series $b_{02}(t)$ for a two-dimensional truncated symmetric convection run at $Ra = 100Ra_c$, $\sigma = 6.8$, $\lambda = 2\sqrt{2}$, $\bar{M} = P = 19$. The initial condition is as in figure 1. (b) $\log \tilde{b}_{02}(f)$; (c) $\langle T \rangle (z, t)$ versus z at two times differing by one-half of the short oscillation shown in (a). The frequency of this oscillation seems to be the Brunt–Väisälä frequency of the stable core of the $\langle T \rangle (z)$ profile.
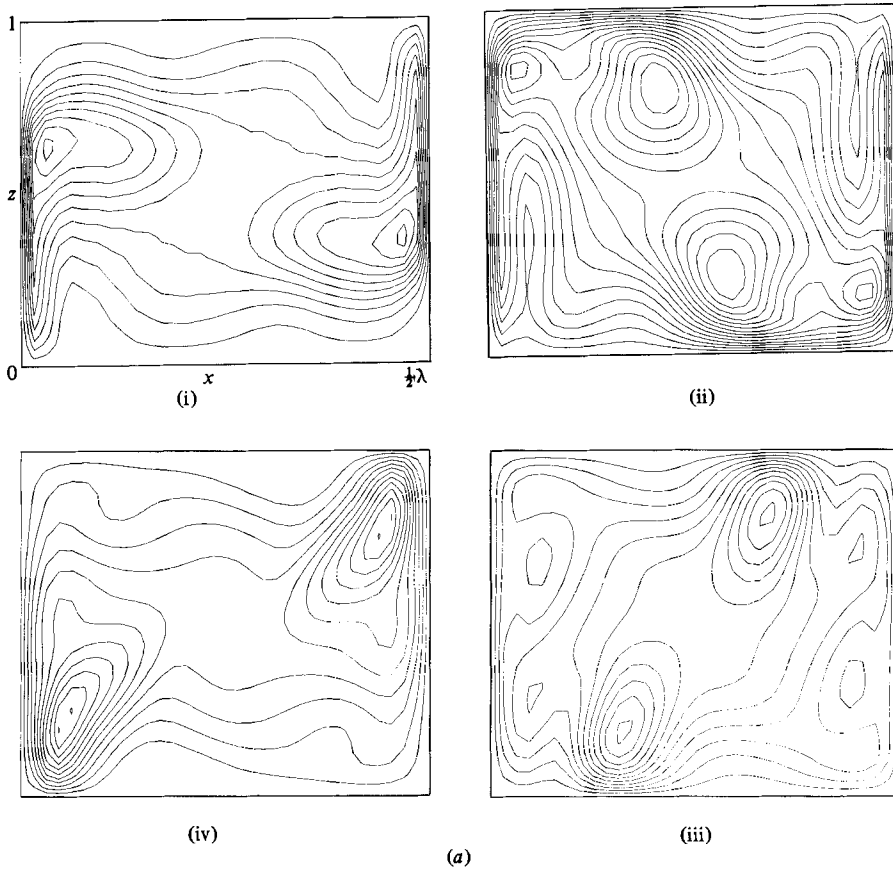
FIGURE 8(*a*). For caption see facing page.

sufficiently high *Ra* three-dimensional excitations overcome the magnetic field constraint.

In figure 10 we plot contours of various components of the flow field. That is, we spectrally decompose the time-dependent flow as

$$v(x, t) = \int u(x, f) \, e^{i2\pi f t} \, df$$

and plots contours of $u(x, f)$ for various frequencies f. The plots in figure 10 are constructed for $f = 0, f_1, f_2, f_3$, where f_1 is the most-energetic frequency (see figure 9), $f_2 = \frac{1}{2} f_1$ is its subharmonic, and f_3 is the low-frequency period ($f_3 \approx \frac{1}{40} f_1 \approx 10$). The plots for $f = 0$ show the mean field through an oscillation cycle.

Again, the frequency f_1 may be identified as the Brunt–Väisälä frequency of the stable core of the mean temperature profile when the flow is not undergoing one of its long-period transitions (see figure 9f). While we cannot yet explain the physics of the oscillation at the low frequency f_3, it may be significant that the flow component responsible for this oscillation is nearly a standing wave and $f_3 \approx \sigma$, the viscous diffusion frequency.

The Poincaré maps plotted in figures 9(h, i) suggest that this flow is not strongly chaotic. As the orbit evolves, the curves in these Poincaré maps are filled alternately
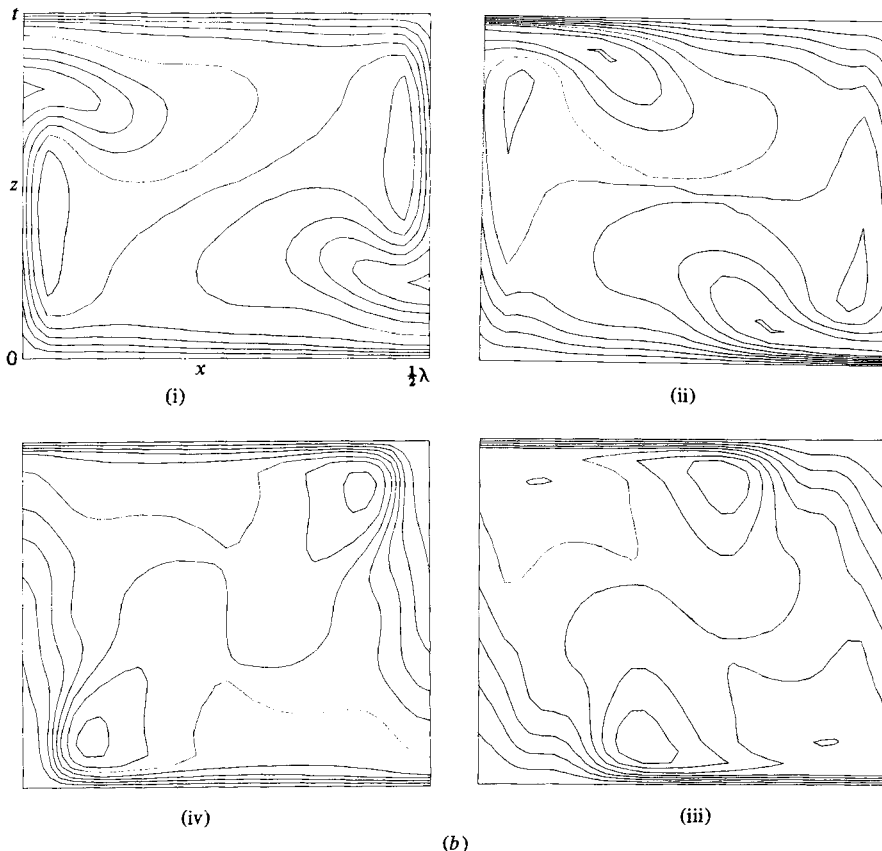
FIGURE 8. Contour plots of vorticity and total temperature for the symmetric convection run with $Ra = 400Ra_0$, $\sigma = 6.8$, $\lambda = 2\sqrt{2}$, $\overline{M} = P = 40$. (a) (i)–(iv): vorticity contours at $t = 0$, $\frac{1}{4}$, $\frac{1}{2}$, $\frac{3}{4}$ respectively of the short time period seen in the time-series plots in figure 9 (b) (i)–(iv): contour plots of total temperature at $t = 0$, $\frac{1}{4}$, $\frac{1}{2}$, $\frac{3}{4}$ respectively of the short time period. Observe that the vortex cores (a) and hot and cold blobs (b) require two of the short oscillation periods to circulate around the box.

on opposite sides, apparently because of the significant excitation at the subharmonic f_2. While the structure of the Poincaré maps is not highly chaotic, we cannot rule out weak chaos that may be producing slight jiggling of the computed points.

As Ra increases further, the two-dimensional Boussinesq system seems to undergo a reverse transition to single-frequency periodic convection at $Ra_1' \approx 800Ra_c$. In figure 11 we plot the time series and power spectra at $Ra = 1000Ra_c$. Observe the simple line structure of the power spectra. No more-complicated behaviour is found at higher Ra with the symmetries imposed. The reverse transition to simply periodic convection is similar to that found in the Lorenz model.

When the lower Prandtl number $\sigma = 1$ is used, fully resolved calculations with the two-dimensional Boussinesq equations (assuming the symmetries (2.12) and (2.13)) seem to give only steadily convecting states (cf. figure 4). No instabilities to even single-frequency periodic convection have yet been found.

While we have not found evidence of chaotic behaviour in two-dimensional Bénard convection, it is possible that chaos may appear in this system if large-aspect-ratio flows are considered. Our results reported here are restricted to aspect ratio $\lambda = 2\sqrt{2}$.
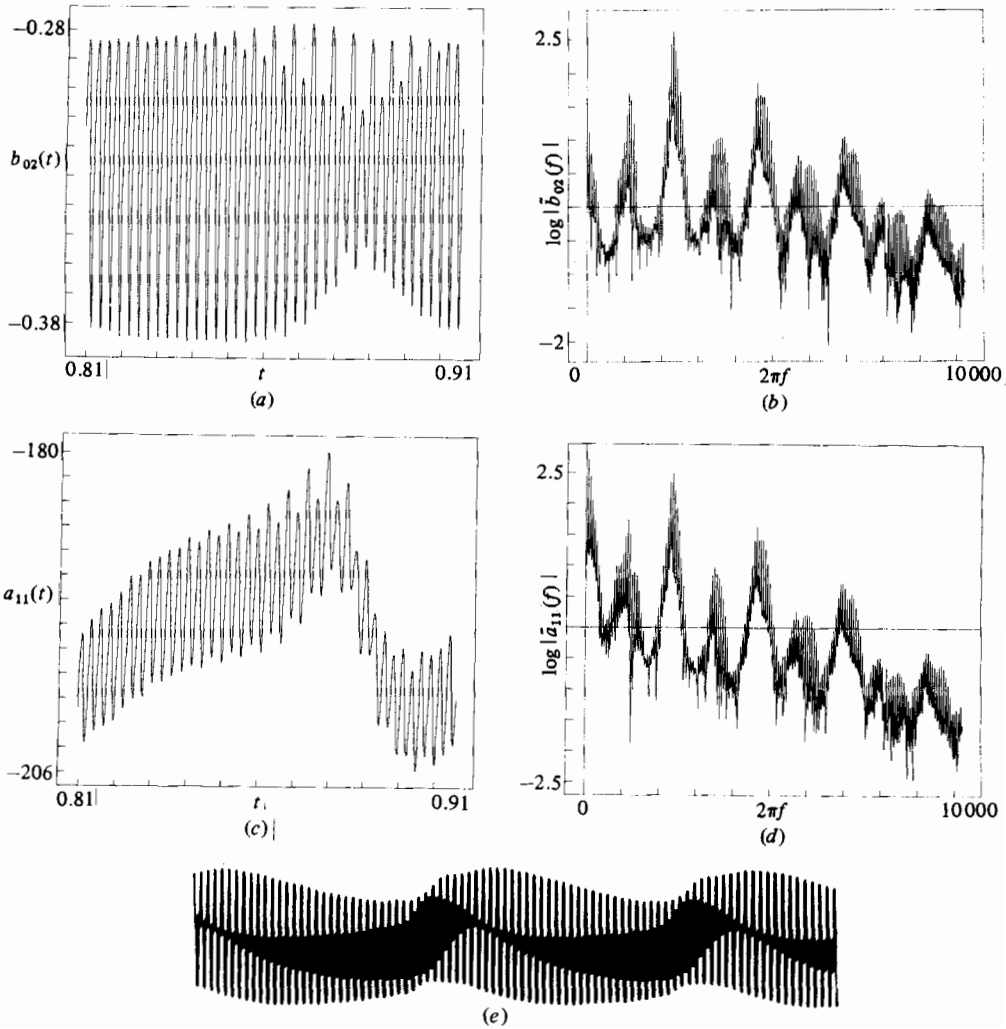
FIGURE 9 (*a–e*). For caption see facing page.

At larger aspect ratios λ, chaos may appear as slow oscillations of convection cell size and location. This possibility requires further investigation by direct numerical solution of the Boussinesq equations. In addition, it should also be stressed that, in more complicated systems like doubly diffusive convection (Moore *et al.* 1983), chaos may develop even in two space dimensions.

5. Three-dimensional results

5.1. *Initialization procedure and description of runs*

Three-dimensional, as opposed to two-dimensional, convection may develop vertical vorticity through the interplay of the buoyancy and the nonlinear terms. This isotropization of vorticity by nonlinearity plays an important role in the development of turbulence in the flow. Indeed, results for three-dimensional convection without significant vertical vorticity (for example with square or cylindrically symmetric cells) have the attributes of two-dimensional convection, including kinetic energy locked into the largest scales.
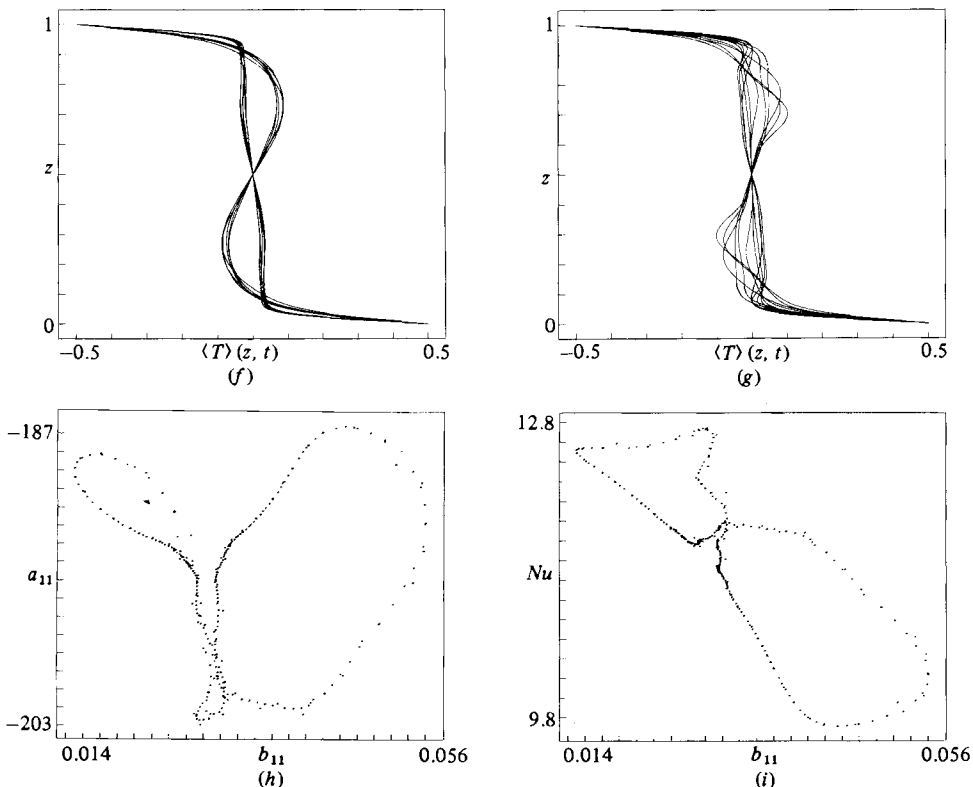
FIGURE 9. Time series, time spectra and Poincaré maps for the symmetric convection run at $Ra = 400Ra_c$, $\sigma = 6.8$, $\lambda = 2\sqrt{2}$: (a) $b_{02}(t)$; (b) $\log b_{02}(f)$; (c) $a_{11}(t)$; (d) $\log a_{11}(f)$. The spectra plotted in (b, d) are computed over six of the long periods $\Delta t \approx 0.10$ of the time series plotted in (a, c). The line structure of the spectra is due to the periodic character of the time series over this long period. (e) Time series observed by Libchaber and coworkers in three-dimensional magnetohydrodynamic convection at magnetic field $B = 1.15$ G, $Ra = 6.76Ra_c$. For $Ra \lesssim 6.7Ra_c$, single-frequency periodic two-dimensional convection is observed, while for $Ra \gtrsim 6.8Ra_c$ chaotic three-dimensional convection is found. At this intermediate Rayleigh number we observe a close simularity to the time series plotted in (a, c). (f) $\langle T\rangle(z)$ versus z at various times separated by one-half the short period observed in (a, c), but outside the times in which a_{11} undergoes the rapid transition observable in (c). (g) $\langle T\rangle(z)$ versus z plotted every half short period during the period of rapid transition of a_{11}. (h, i) Poincaré maps of a_{11} versus b_{11} when $b_{02} = -0.32$, $\mathrm{d}b_{02}/\mathrm{d}t > 0$ and Nusselt number Nu versus b_{11} when $b_{02} = -0.32$ with $\mathrm{d}b_{02}/\mathrm{d}t > 0$ respectively.

To initialize our three-dimensional runs we generate the fields $(v(x, 0),\ T(x, 0))$ as uncorrelated Gaussian data with prescribed spectra. This procedure is analogous to that used in isotropic turbulence calculations (Orszag & Patterson 1972; Herring & Kerr 1982). The energy spectrum $E(k)$ is of the form

$$E(k) = Ak^2\,\mathrm{e}^{-Bk^2}, \tag{5.1}$$

where $B = 0.05$, and A is chosen so that the total kinetic energy is $E_{\mathrm{tot}} = \frac{3}{2}$. The motivation for choosing to initialize the three-dimensional runs with a random flow field is based on our experience with three-dimensional transition runs. In contrast with two-dimensional flows, three-dimensional flows do exhibit chaotic behaviour so we will present statistical measures of the resulting turbulence. However, in order to achieve a statistically nearly stationary state in these turbulent runs it is best to choose random initial conditions. In the non-chaotic transitional regime it seems that
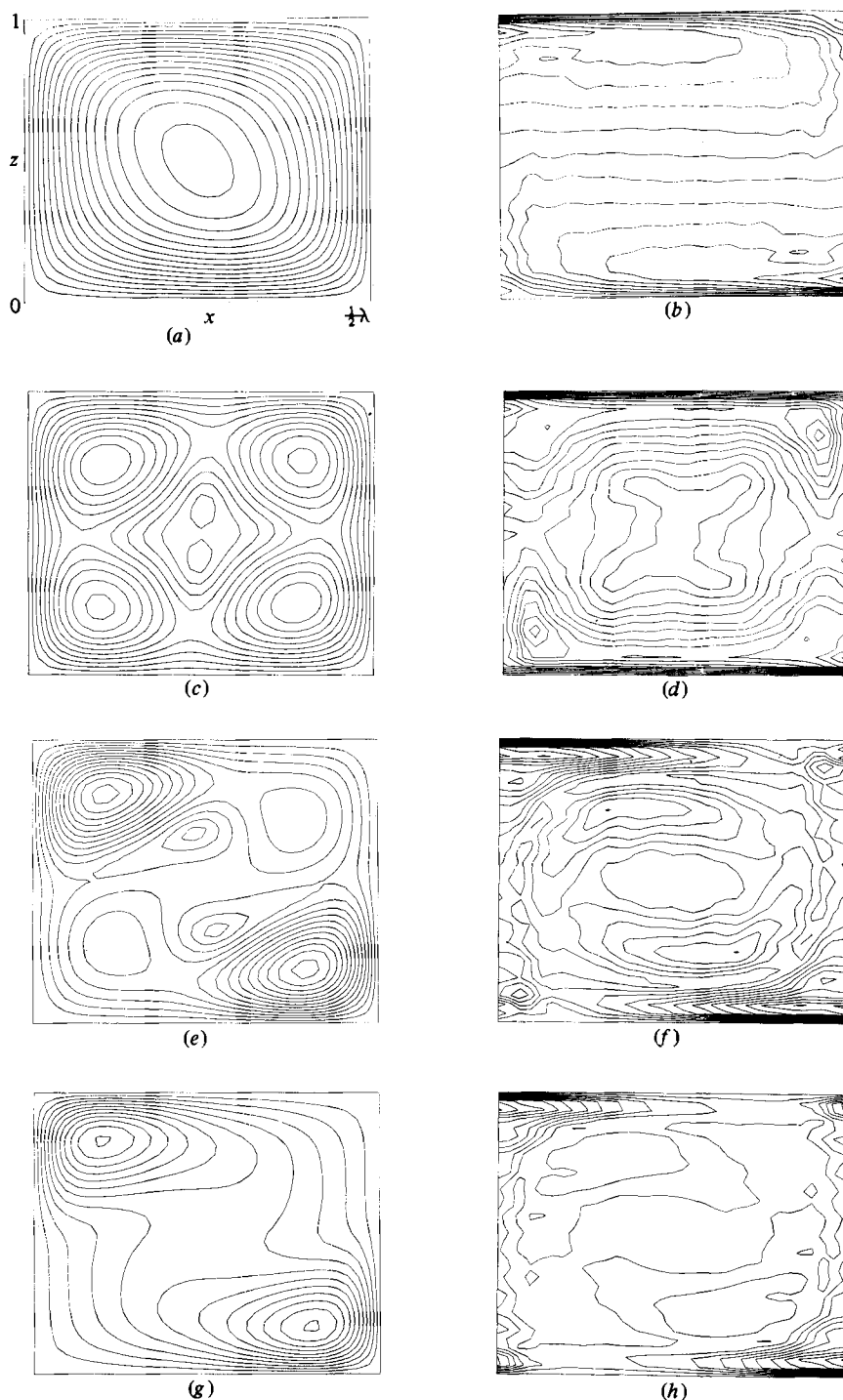
FIGURE 10. Contour plots of stream function and total temperature for the run at $Ra = 400Ra_c$, $\sigma = 6.8$, $\lambda = 2\sqrt{2}$. (a) Mean stream function. (b) Mean total temperature. (c) Stream-function amplitude contours for the flow component oscillating with frequency f_1. (d) Total temperature amplitude for the flow component oscillating at frequency f_1. (e) Stream-function amplitude contours at the subharmonic frequency f_2. (f) Total temperature amplitude contours for f_2. (g) Stream-function amplitude contours at the low frequency f_3. (h) Total temperature amplitude contours at f_3.
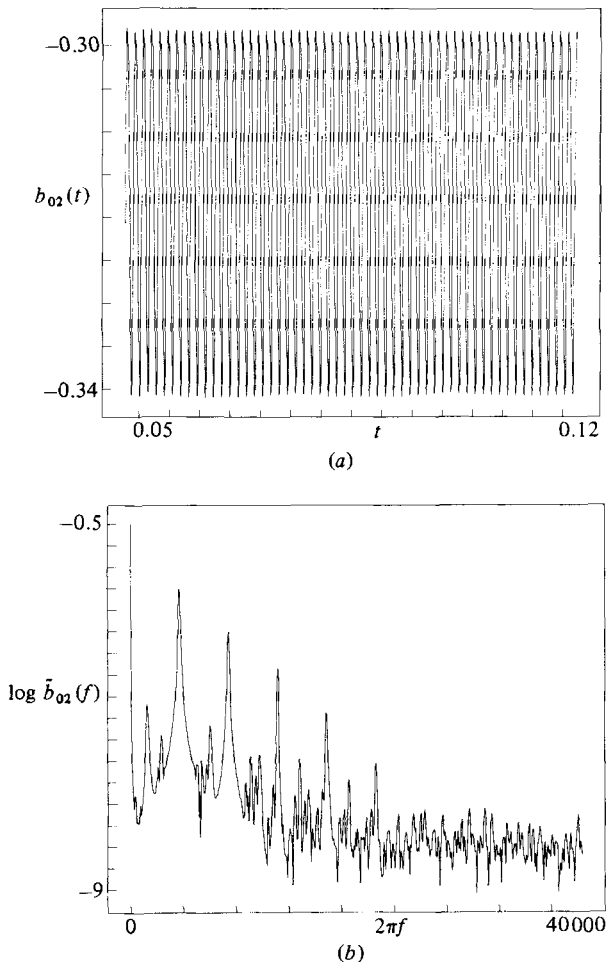
FIGURE 11. Time series of $b_{02}(t)$ (a) and its time spectrum $\log \hat{b}_{02}(f)$ (b) for the symmetric convection run at $Ra = 1000Ra_c$, $\sigma = 6.8$, $\bar{M} = P = 40$. This flow has reverted to a purely oscillatory state. It seems that $Ra'_1 \approx 800Ra_c$ for symmetric convection.

we can still recognize the basic transitional frequencies in such randomly initialized runs.

We designate a three-dimensional run with resolution (M, N, P) (see (2.11)) by simply prefixing this triad with the value of Ra/Ra_c for the run. Thus $70(16^3)$ designates a run for which $Ra/Ra_c = 70$, and $M = N = P = 16$, while $70(32^2 \times 16)$ designates $M = N = 32$, $P = 16$, $Ra/Ra_c = 70$. The runs investigated in this section are at $\sigma = 10$, with the exception of those in §5.4, for which $\sigma = 1$. In addition, we choose $\lambda = \mu = 2\sqrt{2}$ in all the following runs.

5.2. *Results for three-dimensional transition*

Our results concerning transition are presented using both a series of 16^3 and $32^2 \times 16$ runs. At the end of this subsection we examine the numerical accuracy of the $70(32^2 \times 16)$ run by comparing with a single $70(32^3)$ run. The convergence question is not completely settled here; the $32^2 \times 16$ runs do show some wavenumber-truncation errors at high k, especially for the dissipation of the temperature field. However, a
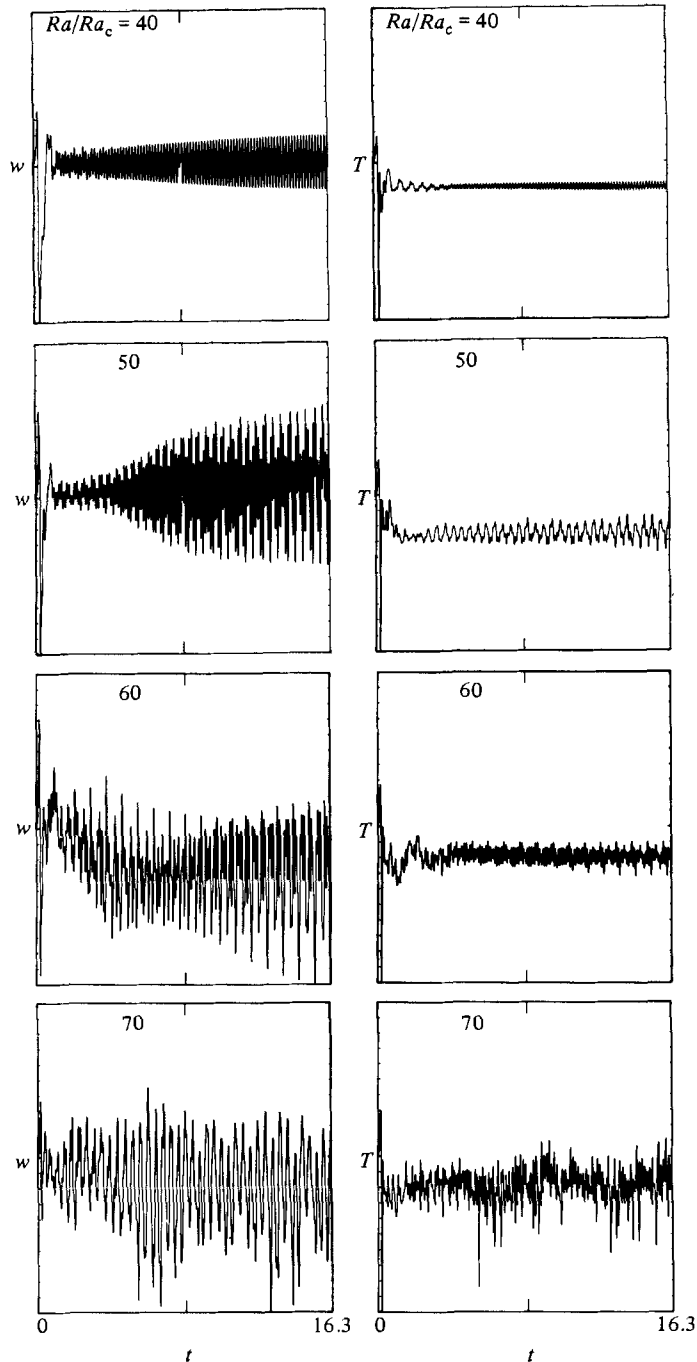
FIGURE 12. Time series for $(w(\boldsymbol{p}, t), T(\boldsymbol{p}, t))$ for resolution 16^3 runs. Here $\boldsymbol{p}$ denotes the coordinate of a point near the middle of the convection box. The four cases shown are $Ra = (40, 50, 60, 70)\ Ra_c$. All runs are initialized using the same random number seed, as described in the text. Note the progressive increase of noisiness in the w and, especially, T time series as Ra/Ra_c increases.

full study of the transition problem at 32^3 is at present prohibitively costly, even on a Cray-1 computer.

Our results suggest the following transition sequence: at 16^3 resolution, the transition towards chaos proceeds from a single-frequency oscillation at $Ra \approx 40Ra_c$ to a two-frequency quasi-periodic state $(45Ra_c \lesssim Ra \lesssim 55Ra_c)$, and then to a multifrequency phase-locked regime $(55Ra_c \lesssim Ra \lesssim 65Ra_c)$, followed by a chaotic state $(Ra \gtrsim 70Ra_c)$. On the other hand, the better resolved $32^2 \times 16$ and 32^3 runs appear to have no phase-locked periodic regime; instead they have an harmonically rich behaviour qualitatively indistinguishable from the chaotic state at larger Ra. The quasi-periodic regime in the $32^2 \times 16$ runs appears considerably more noisy than 16^3 runs at the same Ra, σ; the 16^3 results are presented here solely to elucidate further the dynamics of a relatively low-order spectral system, not because they provide an accurate representation of the physics of the system.

In figure 12 we plot the time series of the temperature field as computed by numerical solution of the three-dimensional Boussinesq equations with $M = N = P = 16$ (see §§2 and 5.3), with random initial data as described above. Power-spectral densities for temperature and vertical velocity are given in figure 13. For $Ra/Ra_c < 35$ a steady convecting roll state is attracting. At $Ra/Ra_c \approx 40$ periodic motion with a non-dimensional frequency of 39 develops at large time. Note that this Ra is consistent with the results of Busse (1972) for the onset of oscillatory instability rolls: $Ra/Ra_c \approx 0.31\sigma^2 + 1$. At $Ra/Ra_c \approx 50$ this periodic oscillation is replaced by a quasi-periodic motion having two incommensurate frequencies $f_1 \approx 45.2$ and $f_2 \approx 13.5$ (see figure 13). All other peaks that appear in the spectra are of the form $m_1 f_1 + m_2 f_2$, where m_1 and m_2 are integers.

For $Ra/Ra_c = 60$ the plots in figures 12 and 13 indicate that the motion is phase-locked and all peaks in the spectra are multiples of the single frequency $f_L \approx 7.1$. This phase-locked state seems to be achieved when the ratio of the two frequencies f_1 and f_2 increases to $f_1/f_2 = \frac{10}{3}$. In the associated temperature spectrum plotted in figure 13 (at $Ra = 60Ra_c$) it is possible to distinguish pairs of spectral peaks which are very close to splitting. This observation suggests that the system is about to exit its phase-locked regime. For $Ra/Ra_c \lesssim 60$ the seemingly chaotic low-amplitude background to the periodic spectra is likely to be due to our processing of the time series and not to fluid turbulence. As Ra/Ra_c increases from 60 to 65, the frequency spectra again exhibit two incommensurate frequencies $\hat{f}_1 \approx 7.35$ and $\hat{f}_2 \approx 8$. Both $\hat{f}_1$ and $\hat{f}_2$ are close to the fundamental locking frequency f_L at $Ra/Ra_c = 60$. At $Ra/Ra_c = 65$ the flow seems slightly chaotic.

Finally at $Ra/Ra_c = 70$ the temperature spectrum is noisy and quite broad, although a sharp spectral line is still visible in the velocity spectrum. However, even for the velocity field, the background noise level has increased by at least two orders of magnitude. The relative noisiness of the temperature compared to the velocity is apparently due to the high Prandtl number of the fluid.

In figure 14 we present two-dimensional phase projections of the 16^3 orbits at various Ra. The curves show $u(\boldsymbol{p}, t)$ versus $w(\boldsymbol{p}, t)$ (where $\boldsymbol{p}$ is a coordinate near the midpoint of the box) for $3 \leqslant t \leqslant 4$. The two plots at $Ra = 60Ra_c$ are obtained for different initial conditions, showing dependence of the final quasi-periodic state on initial data. This difference may also suggest alternative routes to chaos, in addition to the Ruelle *et al.* scenario described in §1. At $Ra = 65Ra_c$ the phase portrait in figure 14 suggests a chaotic flow although the spectrum of the flow is still dominated by phase-locked lines. Only the velocity components have phase plots that project onto a torus; those that involve the temperature appear much more random.
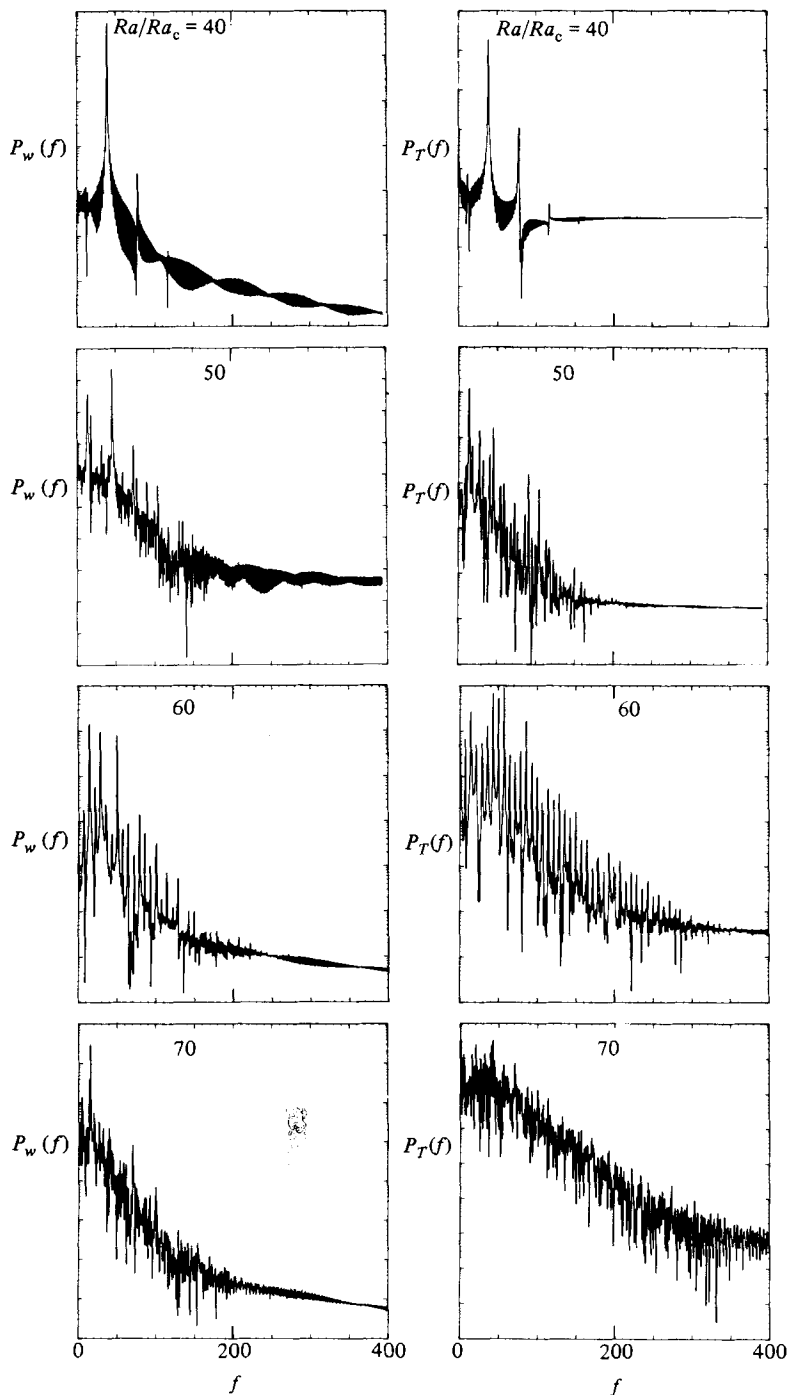
FIGURE 13. Power-spectral densities for the $(w(\boldsymbol{p}, t),\ T(\boldsymbol{p}, t))$ fields whose time series are shown in figure 12. Only the last $\frac{3}{4}$ of the time record is used in the Fourier analysis in order to eliminate the initial transient.
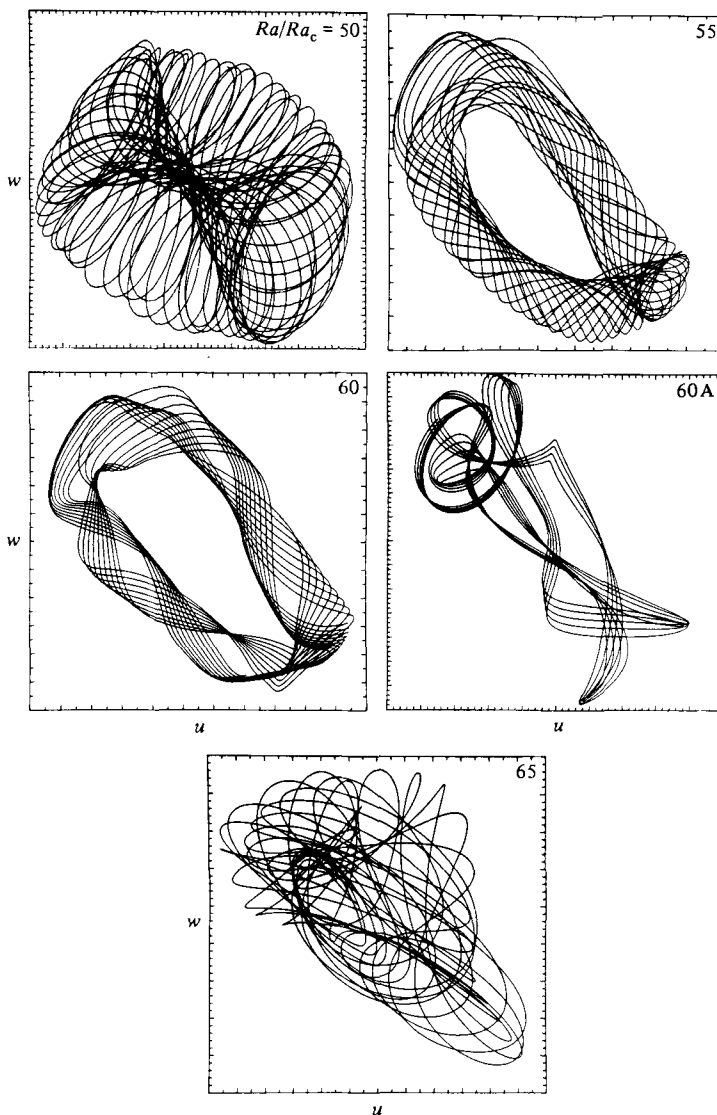
FIGURE 14. Two-dimensional phase projections of the $(u(\boldsymbol{p}, t)$, $w(\boldsymbol{p}, t))$ fields for the same runs as described in figures 12 and 13. The plot marked 60A shows the case $Ra = 60Ra_c$ for a slightly different initial random seed, and illustrates dependence of the final quasiperiodic state on the initial data. Also shown is the case $Ra = 65Ra_c$ which suggests a slightly chaotic flow, although the power spectra appear dominated by two frequency components.

In figures 15 and 16 we present time series and power spectra for the $32^2 \times 16$ system, which may be compared with the results plotted in figures 12 and 13 respectively for the 16^3 mode system. We notice a marked attenuation of high-frequency power, but an increased randomness of the surviving low-frequency components, particularly near $Ra = 60Ra_c$. Analysis of the $60(32^2 \times 16)$ case is especially difficult because of the long initial transient ($t \approx 8$), during which the temperature fluctuations are unusually small. Apparantly $Ra = 60Ra_c$ is close to a transition to a more-chaotic state. Comparing again with figures 12 and 13, we note that the quasi-periodic regime near $Ra = 55Ra_c$ is considerably noisier than the 16^3
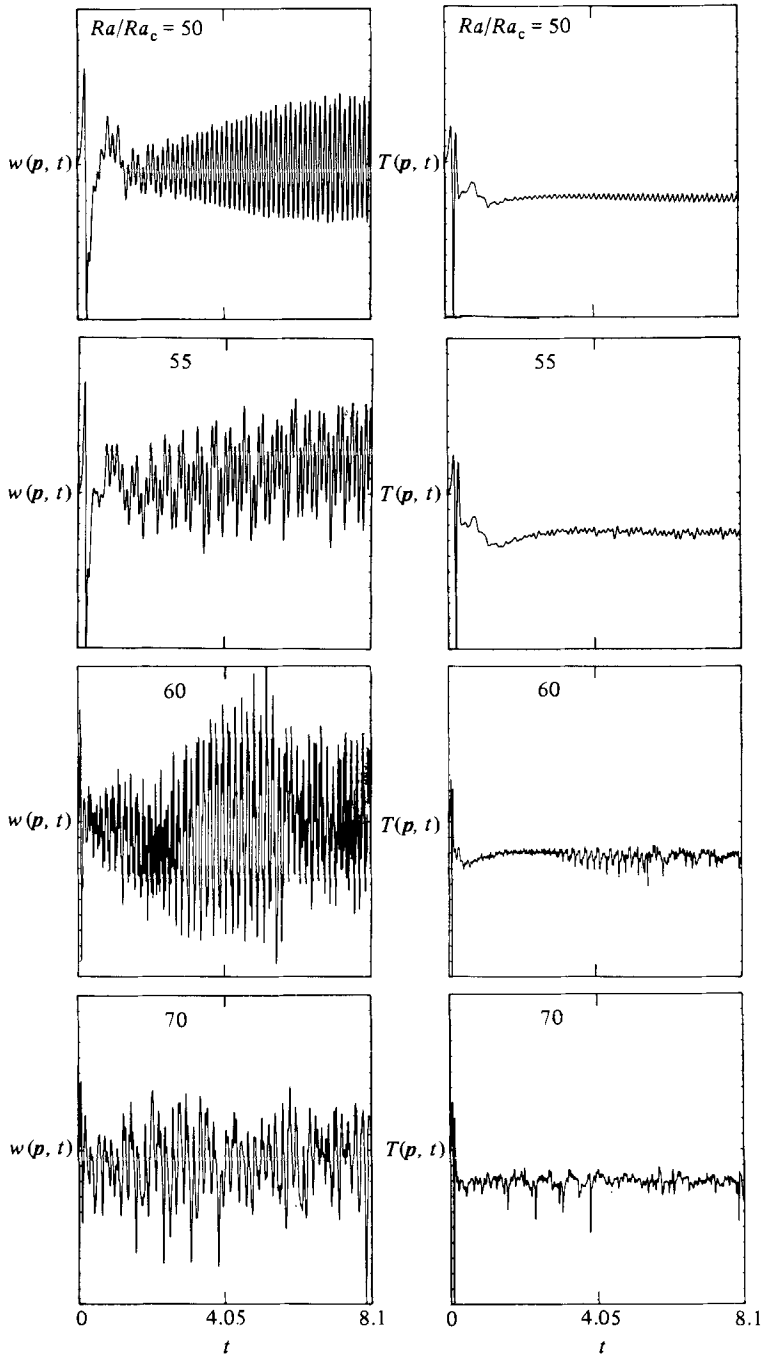
FIGURE 15. Time series for $(w(\boldsymbol{p}, t), T(\boldsymbol{p}, t))$ for $32^2 \times 16$ runs. Except for increased resolution, these runs are identical with those described in figures 12–14. Note the strong attenuation of high frequencies as compared with the time series of figure 12, indicating inadequate resolution of the 16^3 runs, except at $Ra = (40, 50) \, Ra_c$.
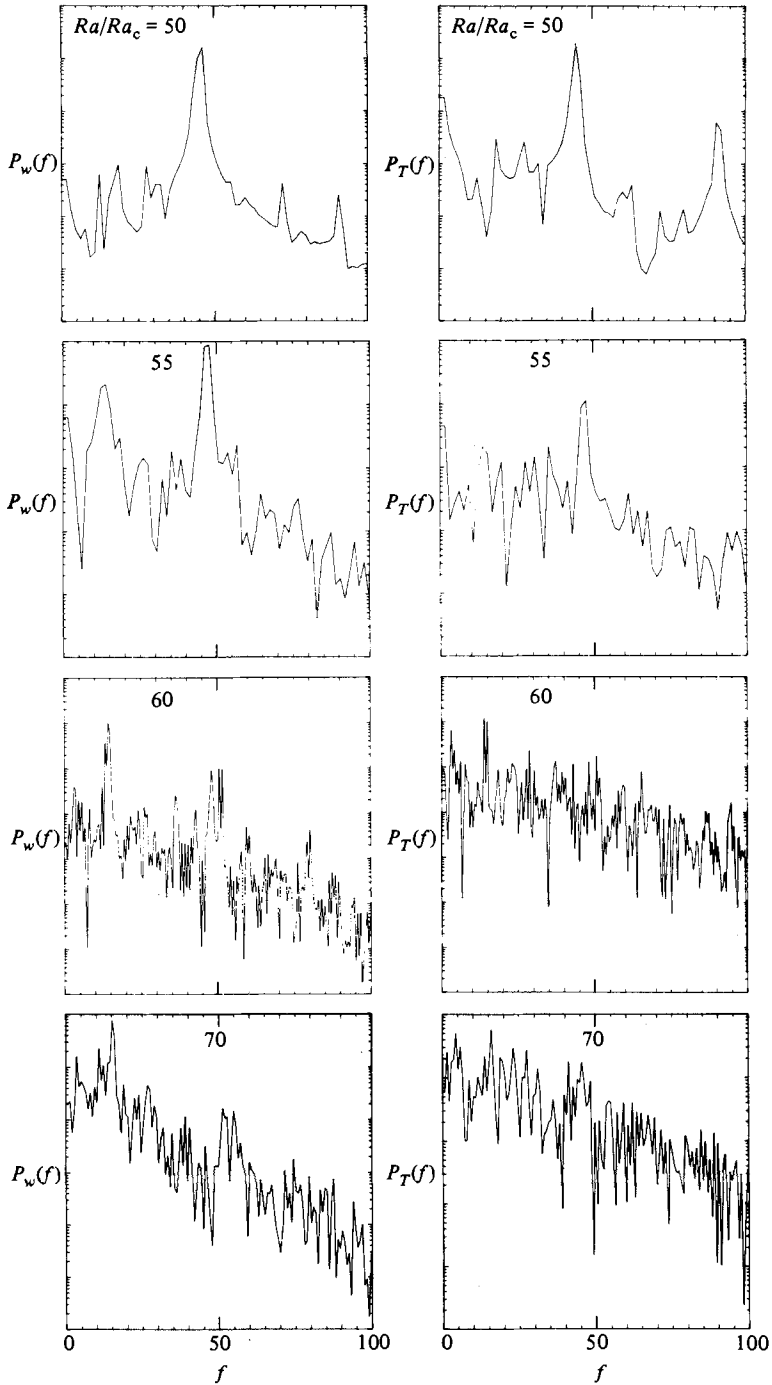
FIGURE 16. Power spectra for $(w(\boldsymbol{p}, t),\ T(\boldsymbol{p}, t))$ for resolution $32^2 \times 16$ during the latter $\frac{3}{4}$ of the time record. For $Ra = 60 Ra_c$ the increased resolution relative to the run whose results are plotted in figure 13 appears both to attenuate the high frequencies and to increase the 'randomness' of the surviving low-frequency components.
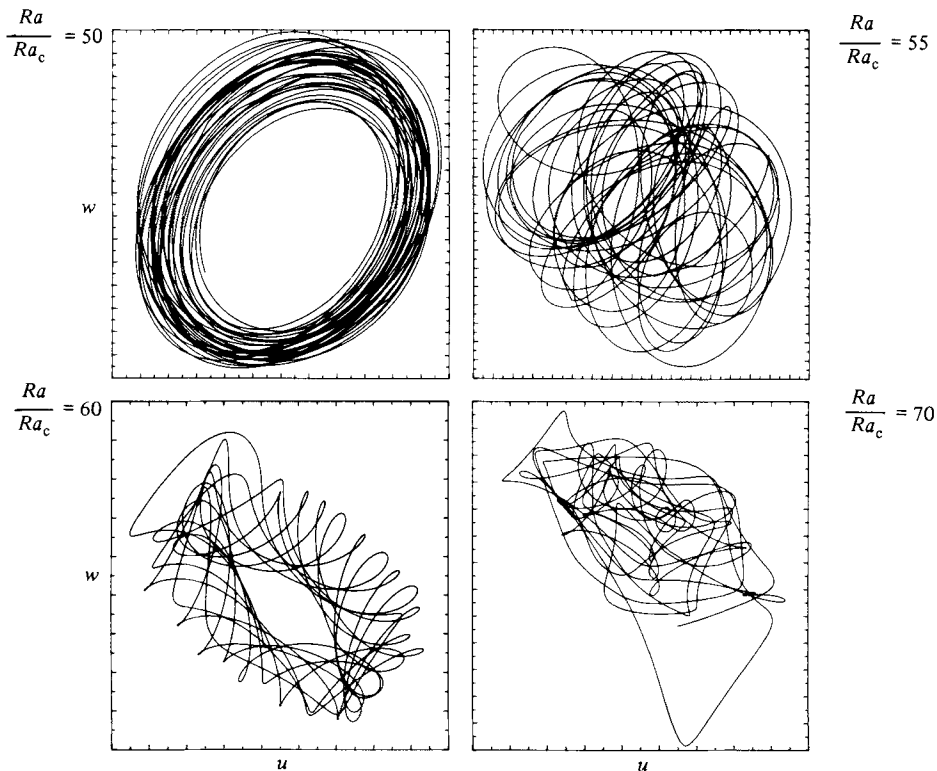
FIGURE 17. Phase plots for $(u(\boldsymbol{p}, t),\; w(\boldsymbol{p}, t))$ at resolution $32^2 \times 16$. Except for resolution, the conditions of these runs are the same as those of figure 14. In comparison with the equivalent low-resolution runs (see figure 14) we note the apparent absence at $Ra/Ra_c = 50$ of the two frequencies, and the less well-defined two-frequency regime at Ra/Ra_c.

results; it is much more difficult to discern any possible phase-locked behaviour in the range $60Ra_c \leqslant Ra \leqslant 65Ra_c$. Notice that the $50(32^2 \times 16)$ run appears still to be primarily a single-frequency flow as opposed to the $50(16^3)$ run, which has already bifurcated to two frequencies.

In figure 17 selected phase plots are given for the $32^2 \times 16$ runs at $Ra = (50,\ 60,\ 70)\ Ra_c$. In contrast with the 16^3 results plotted in figure 14, the plot of $(u(\boldsymbol{p}, t), w(\boldsymbol{p}, t))$ at $50Ra_c$ is now a simple circle, corresponding to the presence of only a single frequency. The phase plot at $Ra = 60Ra_c$ has much the same appearance as with 16^3 resolution. At $Ra = 70Ra_c$ we again observe a chaotic regime. The transition scenario reported here for three dimensions closely parallels route I described by Gollub & Benson (1980). The qualitative differences are related to the existence or non-existence of phase-locked regimes, although such regimes may be present for some range of parameters, they are not observed by us because of the coarseness of our slice through parameter space.

We now examine the accuracy of the $32^2 \times 16$ run at the highest Ra considered ($70Ra_c$), since at this Ra convergence should be poorest. This issue is considered both from the perspective of contour plots of the various fields and time series of the fields at a particular point. In figure 18 contour plots of the temperature field are given at $t = 4$ for the three resolutions 16^3, $32^2 \times 16$ and 32^3. Both horizontal and vertical slices are shown. Notice that for the 16^3 runs the ascending and decending plumes are ill defined and are accompanied by apparently spurious, closed, small-scale
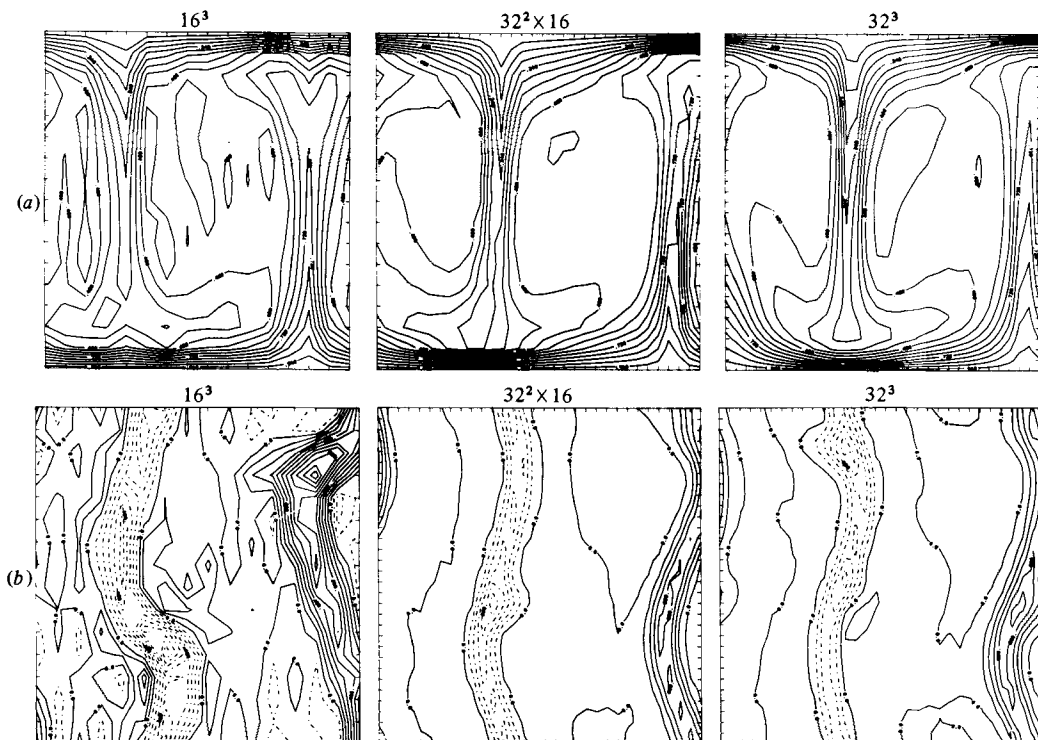
FIGURE 18. Comparison of contour plots of the $T(x, t)$ field for resolutions 16^3, $32^2 \times 16$ and 32^3 at $Ra = 70Ra_c$ and $t = 4.0$. (a) Vertical ($x = 0.5\lambda$) slices; and (b) horizontal ($z = 0.5$) slices. The numerical spatial noise in the 16^3 runs appears as high-frequency noise in figure 13.

temperature contours, indicating poor resolution. On the other hand, the $32^2 \times 16$ fields are much more reasonable, with well-defined plumes extending over the whole core region of the flow. The latter fields still do not resolve well the temperature dissipation in the core region, but the contribution of this term to the entropy budget is small.

In figure 19 time series are plotted for $T(p, t)$ ($0 \leqslant t \leqslant 4$) for the three resolutions. The $32^2 \times 16$ run remains well correlated with the 32^3 run during the entire timespan (especially for low-to-moderate frequency features), but the 16^3 run rapidly decorrelates for both v and T fields. At long times the (v, T) fields for $32^2 \times 16$ and 32^3 must diverge if the flow is intrinsically unpredictable. Estimates for the time of unpredictability are a few large-scale turnover times (Leith & Kraichnan 1972).

The good agreement between the $32^2 \times 16$ and 32^3 runs shown in figure 19 suggest that $P = 16$ is adequate vertical resolution. While we are less confident that $M = N = 32$ gives adequate horizontal resolution, the contour maps plotted in figure 18 suggest horizontal errors are not too large.

5.3. *Character of the three-dimensional flow at $\sigma = 10$*

We now examine the qualitative aspects of the flow, and present information on how turbulently active the present three-dimensional calculations are relative to experimental flows and previous calculations of homogeneous turbulence. We discuss here only the high-resolution $32^2 \times 16$ and 32^3 results. It is convenient to introduce measures of isotropization, transfer to small scales, and other indicators of nonlinearity such as Reynolds and Péclet numbers.
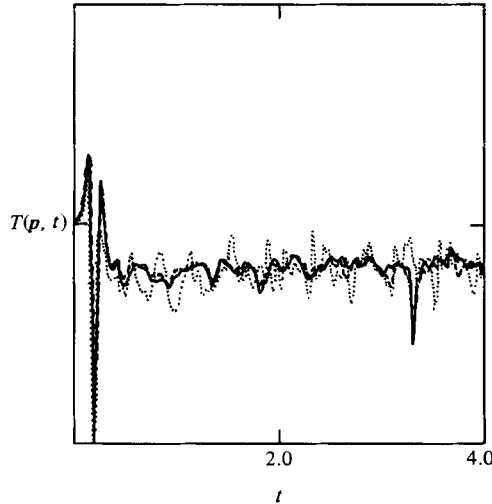
FIGURE 19. Comparison of time series $(0 \leqslant t \leqslant 4.0)$ at $Ra = 70Ra_c$ for the three resolutions 16^3, $32^2 \times 16$ and 32^3 for the temperature fields $T(p, t)$.

The discussion of isotropization is facilitated by the introduction of orthogonal solenoidal unit vectors $e_1(k)$ and $e_2(k)$, defined by

$$e_1(k) = \frac{k \times \hat{z}}{|k \times \hat{z}|} \tag{5.2}$$

and

$$e_2(k) = \frac{k \times e_1(k)}{|k \times e_1(k)|},$$

where $\hat{z}$ is the unit vertical vector. The buoyant acceleration in (2.1) is parallel to $e_2(k)$; velocity components parallel to $e_1(k)$ must either be present in the initial data or be activated by nonlinear interactions in (2.1). Conversely, if buoyancy is absent, nonlinear mixing will lead to equipartition of energy of $u(k, t)$ along $e_1(k)$ and $e_2(k)$. A convenient measure of isotropy is thus given by resolving the kinetic energy along these components:

$$\psi_1(t) \equiv \langle |e_1(k) \cdot u(k)|^2 \rangle, \tag{5.3}$$

$$\psi_2(t) \equiv \langle |e_2(k) \cdot u(k)|^2 \rangle, \tag{5.4}$$

where the angular brackets denote an average over the entire periodic volume (a sum over all available wavenumbers). For isotropic turbulence $\psi_1 = \psi_2$, so a gross measure of the departure from isotropy is given by

$$I^2 = \psi_1/\psi_2. \tag{5.5}$$

In the absence of anisotropic forcing (and boundaries), the nonlinear terms in the Navier–Stokes equations should lead to isotropization of the flow field. A measure of this rate is given by $(D(\psi_1 - \psi_2)/Dt)_{NL}$, where the subscript NL signifies that only the nonlinear terms $v \cdot \nabla v - \nabla p$ are retained in the dynamics. According to classical turbulence phenomenology (Rotta 1951) and earlier numerical calculations (Schumann & Herrring 1976), the attenuation of anisotropy should proceed at the rate

$$\left(\frac{D(\psi_1 - \psi_2)}{Dt}\right)_{NL} = \frac{C_v E^{\frac{1}{2}}}{L(\psi_1 - \psi_2)}, \tag{5.6}$$

where C_v is a constant, E is the total kinetic energy, L an integral lengthscale, conveniently taken as

$$L = E^{\frac{3}{2}}/\epsilon, \tag{5.7}$$

and ϵ is the kinetic-energy dissipation rate. The presence of slip boundaries must modify these considerations, but the core of the flow remains approximately homogeneous. A relaxation formula similar to (5.6) may also employed for the heat-flux (Nusselt number) Nu

$$\left[\frac{\mathrm{D}(Nu)}{\mathrm{D}t}\right]_{\mathrm{NL}} = C_T \frac{E^{\frac{1}{2}}}{L} Nu. \tag{5.8}$$

If the turbulence is vigorous, we expect an appreciable amount of energy (and entropy) to cascade to scales much smaller than L where dissipation removes them. The Taylor microscale for the velocity field is

$$\lambda_u^2 \equiv \frac{\langle u^2 \rangle}{\langle (\partial u/\partial x)^2 \rangle}, \tag{5.9}$$

where u is a component of the velocity field. Similarly the temperature microscale is

$$\lambda_T^2 \equiv \frac{\langle T'(x)^2 \rangle}{\langle (\partial T'/\partial x)^2 \rangle}. \tag{5.10}$$

Here the primes indicate a deviation from the horizontal average. Microscale Reynolds and Péclet numbers may now be introduced on the basis of the lengthscales (5.7), (5.9), and (5.10):

$$R_L \equiv \frac{\langle u^2 \rangle^{\frac{1}{2}} L}{\nu}, \tag{5.11}$$

$$R_\lambda \equiv \frac{\langle u^2 \rangle^{\frac{1}{2}} \lambda_u}{\nu}, \tag{5.12}$$

$$P_L \equiv \frac{\langle u^2 \rangle^{\frac{1}{2}} L}{\kappa}, \tag{5.13}$$

$$P_\lambda \equiv \frac{\langle u^2 \rangle^{\frac{1}{2}} \lambda_T}{\kappa}. \tag{5.14}$$

Another convenient measure of nonlinear cascade to small scales are skewnesses, defined as

$$S_{uuu} = -\frac{\langle (\partial u/\partial x)^3 \rangle}{\langle (\partial u/\partial x)^2 \rangle^{\frac{3}{2}}}, \tag{5.15}$$

with similar expressions for the (y, z)-directions. For isotropic three-dimensional turbulence at moderate and large R_λ, $S_{uuu} \approx 0.5$. On the other hand, in two dimensions $S_{uuu} = 0$, since S_{uuu} measures the rate of stretching of vorticity, which is zero for two-dimensional flow. For isotropic turbulence, $S_{uuu} \propto \langle v \cdot \nabla^2 (\partial v/\partial t)_{\mathrm{NL}} \rangle$. A similar temperature-transfer-sensitive skewness is

$$S_{uTT} = -\frac{\langle (\partial u/\partial x)(\partial T/\partial x)^2 \rangle}{\langle (\partial u/\partial x)^2 \rangle^{\frac{1}{2}} \langle (\partial T/\partial x)^2 \rangle} \tag{5.16}$$

Again, for isotropic turbulence $S_{uTT} \propto \langle T \nabla^2 (\partial T/\partial t)_{\mathrm{NL}} \rangle$ (Monin & Yaglom 1975).

In figure 20 information on turbulence parameters is plotted, averaged during the statistically stationary, late-time phase of the runs. Notice that S_{uuu} is very small for $Ra \leqslant 50 Ra_c$. The behaviour of S_{uuu} is similar to that for the isotropy ratio I (see
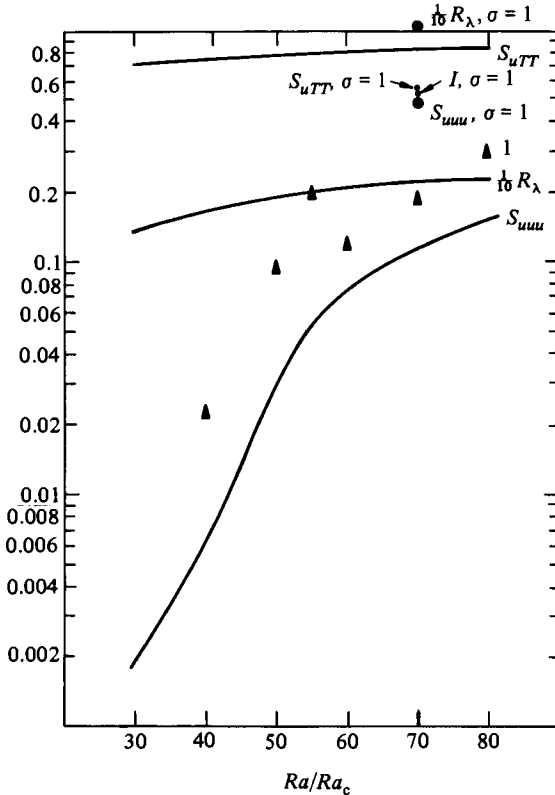
FIGURE 20. Turbulence parameters S_{uu}, S_{uTT}, I and R_λ as functions of Ra/Ra_c during the later portion of the computed time record. These quantities are the velocity skewness (5.15), the mixed temperature skewness (5.16), the isotropy ratio (5.5) (labelled by the points ▲) and the microscale Reynolds number (5.12) respectively. The resolution of runs used here is $32^2 \times 16$. The variation of the isotropy ratio with Ra has a more-complex structure than the other plotted parameters. The solid labelled circles are for a $\sigma = 1$, $Ra = 70Ra_c$ run with identical initial conditions (see §5.4).

(5.5)). In this same Ra-region the (w, T)-probes (displayed in figure 15) indicate a transition from simple harmonic oscillations toward a harmonically richer behaviour. For $Ra/Ra_c = 70$–80, the values of R_λ and S_{uuu} are consistent with the measurements of Tavoularis, Bennett & Corrsin (1978) and the homogeneous turbulence calculations of Herring & Kerr (1982). The values of S_{uTT} are large and near their saturation value for all these runs even for quite small R_λ.

In figure 21 plots are given of the behaviour of the isotropization rates $C_v(t)$ and $C_T(t)$, defined by (5.6) and (5.8) respectively, at $Ra = 60Ra_c$. The behaviour of $C_v(t)$ is quite anomalous for early times $(t \lesssim 10)$ compared with that expected pheno-menologically. Apparently the flow shows little tendency to isotropize in space, except during an event, when isotropization reaches an abnormally large, and short-lived, value. At longer times the amplitudes of these excursions subside and C_v appears to approach an average value of about -3.6. The behaviour of $C_T(t)$ is as expected, and the value obtained, $C_T \approx -0.9$, is in rough agreement with that assumed in turbulence-transport models.

We now turn to a more-detailed consideration of the temporal and spatial behaviour of three-dimensional convection as a function of Ra. The results to be discussed are presented in figure 22, which shows midplane contours of $w(x, t)$, $T(x, t)$,
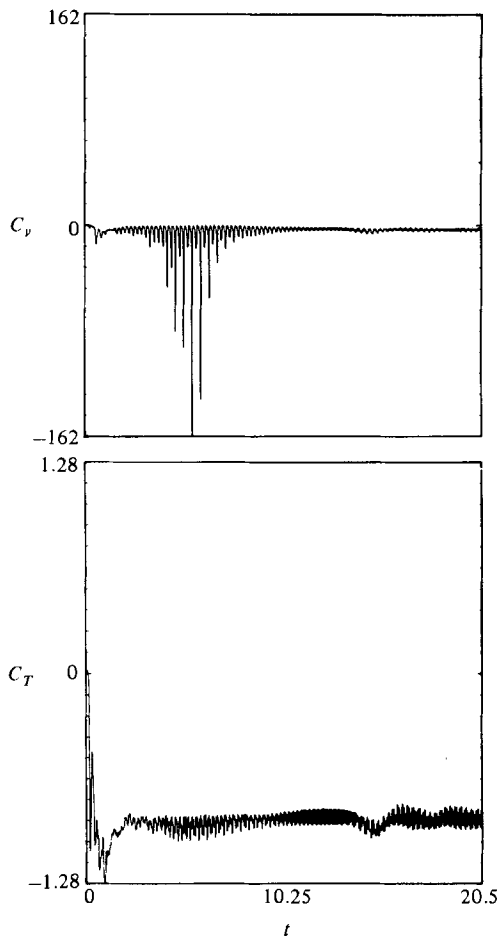
FIGURE 21. Time series for the isotropization rates C_v (5.6) and C_T (5.8) for $Ra = 60Ra_c$ at resolution $32^2 \times 16$. The evolution of $C_v(t)$ is dominated by 'bursts', suggesting little tendency to isotropize except at those times when C_v is unusually large; $C_T(t)$ is more typical of homogeneous turbulence.

$(\nabla \times \boldsymbol{u})_3$ and $\langle T \rangle(\boldsymbol{x}, t)$, as functions of x for runs $40(32^2 \times 16)$, $55(32^2 \times 16)$ and $70(32^2 \times 16)$. These plots were selected as typical during the statistically stationary, late-time period of the convection. We shall postpone temporarily the discussion of the time development of the flow. We first examine the sequence $\langle T \rangle$ as a function of Ra. Note that the core-convection region has a stable temperature gradient, as found in two dimensions (see §4). The stable core region appears typical of quasi-two-dimensional convection. The stable core region appears necessary to retard the convective instability, in the absence of a cascade to large wavenumbers, which is inhibited by the quasi-two-dimensionality. Just for the two-dimensional cases discussed in §4, we find that the most energetic frequency of the periodic and quasi-periodic cases (i.e. $40(32^2 \times 16)$ and $55(32^2 \times 16)$) corresponds closely to the Brunt–Väisälä frequency characteristic of the core region. However, the planform of the oscillations here is three-dimensional. This may be seen in figure 22 (a), which shows the w-contours at the midplane. The motion at $Ra = 40Ra_c$ consists of three-dimensional lenticular plumes imbedded in the core of the two-dimensional rolls. The temporal oscillations concur with a waxing and waning of these lenticular
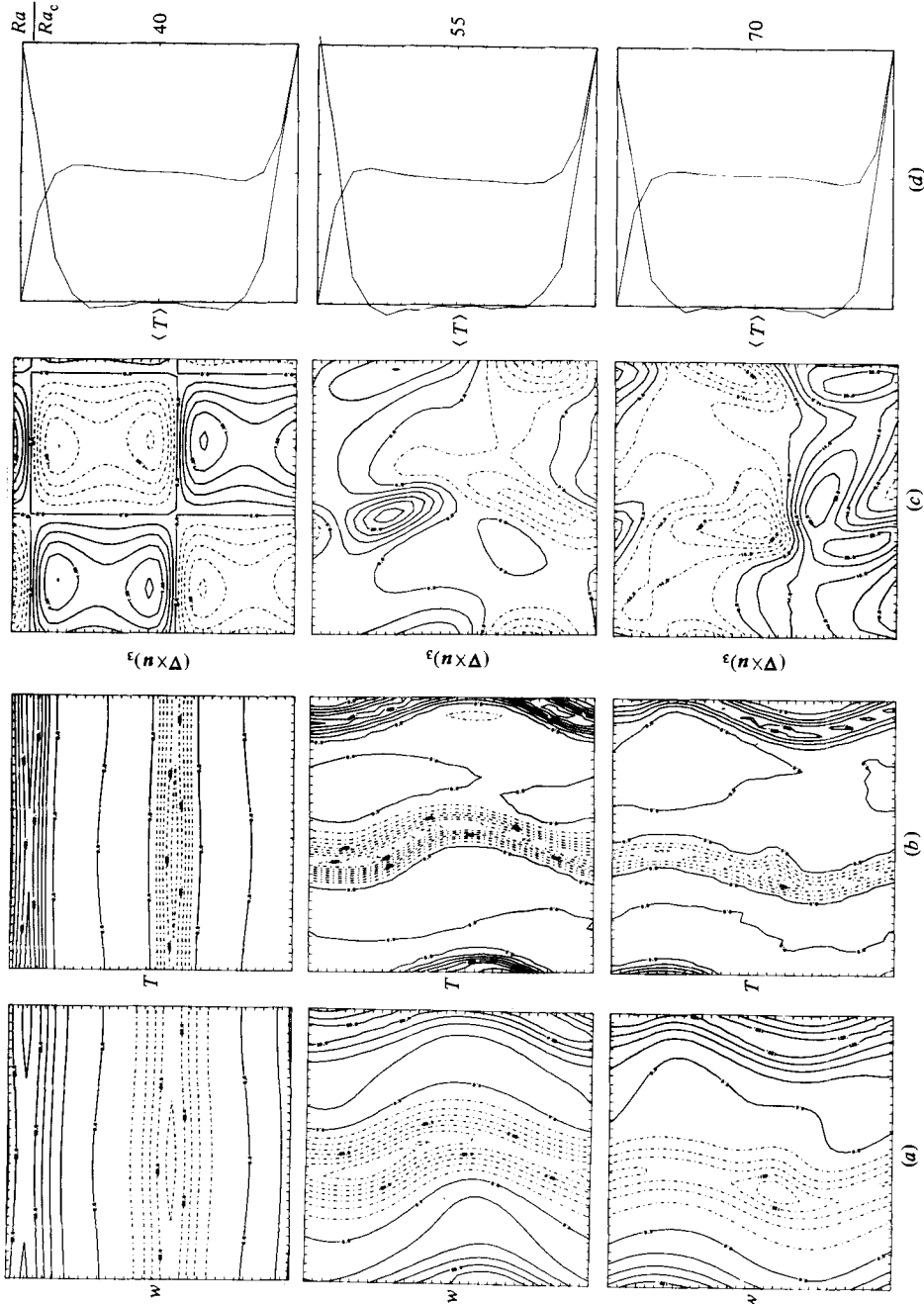
FIGURE 22. Midplane contours of $w(x, y, 0.5, t)$ (series a), $T(x, y, 0.5, t)$ (series b), $(\nabla \times v)_3 (x, y, 0.5, t)$ (series c), and $\langle T \rangle (z, t)$ and $-\partial \langle T \rangle / \partial z$ (series d) for $Ra = (40, 55, 70) Ra_c$. Here $t = 12$, a value sufficiently large that these profiles are typical of the statistically steady state. The angular brackets denote horizontal average. Resolution is $32^2 \times 16$, and $\sigma = 10$. The roll orientation depends sensitively on the initial data.
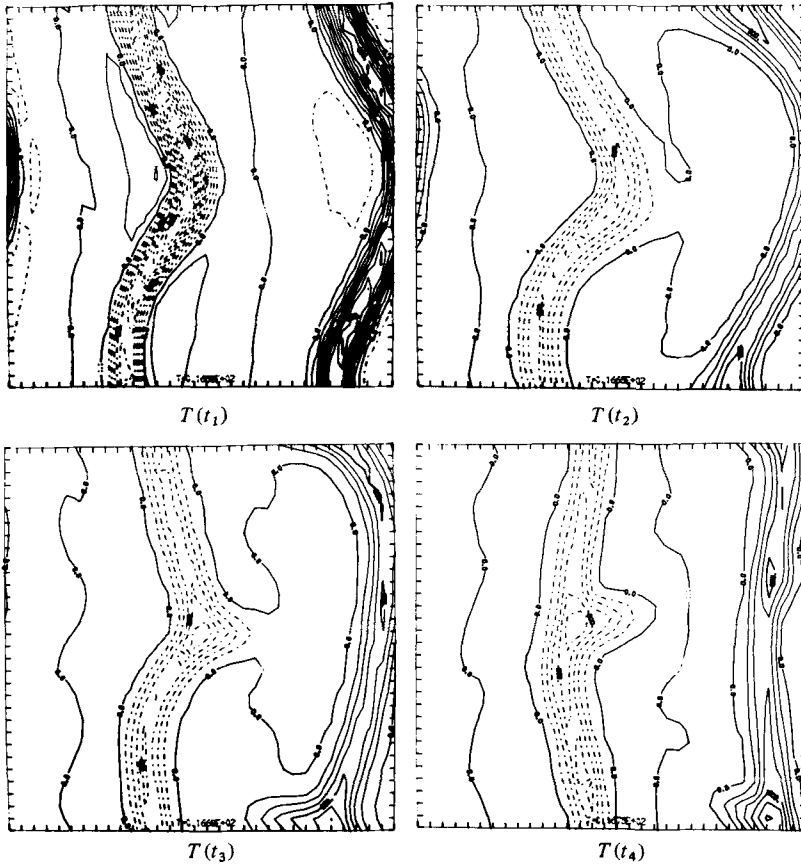
FIGURE 23. Midplane contour plots of $T(x, y, 0.5, t)$ for $t = (17.63, 17.64, 17.65, 17.66)$ for the run $70(32^2 \times 16)$ with $\sigma = 10$. This sequence of contour plots shows the reconnection of zero-temperature lines separating cool from warm fluid.

patterns. From figure 22(c) for the midplane vertical vorticity field we deduce the horizontal convergence needed to support this pattern. Quite similar w-contours have been observed in the calculations of Grötzbach (1982, 1983) and Eidson (1982) with rigid boundaries. The resulting motion gives rise to an asymmetric mean-temperature profile, as shown in figure 22(d). The asymmetry appears as a hot (or cold) anomaly just exterior to the upper or lower boundary layer. The position of this anomaly oscillates from top to bottom at the Brunt–Väisälä frequency.

As Ra is increased from $40Ra_c$ to $50Ra_c$ the roll boundaries begin to execute a sinuous undulation, whose intensity increases with Ra. The frequency of this undulation (which becomes meandering at large Ra) is the lower frequency of the two-component mode described in §5.2. At $Ra = 55Ra_c$ there appears to be some low-level random noise. This noise is manifest in the merging of roll neutral lines, which find themselves in near contact because of the roll-boundary meandering. As these neutral lines separating cool from warm fluid touch they may reconnect so as to allow cool (or warm) fluid to flow horizontally into a more three-dimensional and irregular pattern. The sinuous (meandering at larger Ra) mode has little intensity at $Ra = 50Ra_c$, but its energy becomes dominant at $Ra = 70Ra_c$.

One significant feature of the temperature signal for $70(32^2 \times 16)$ is the sharp
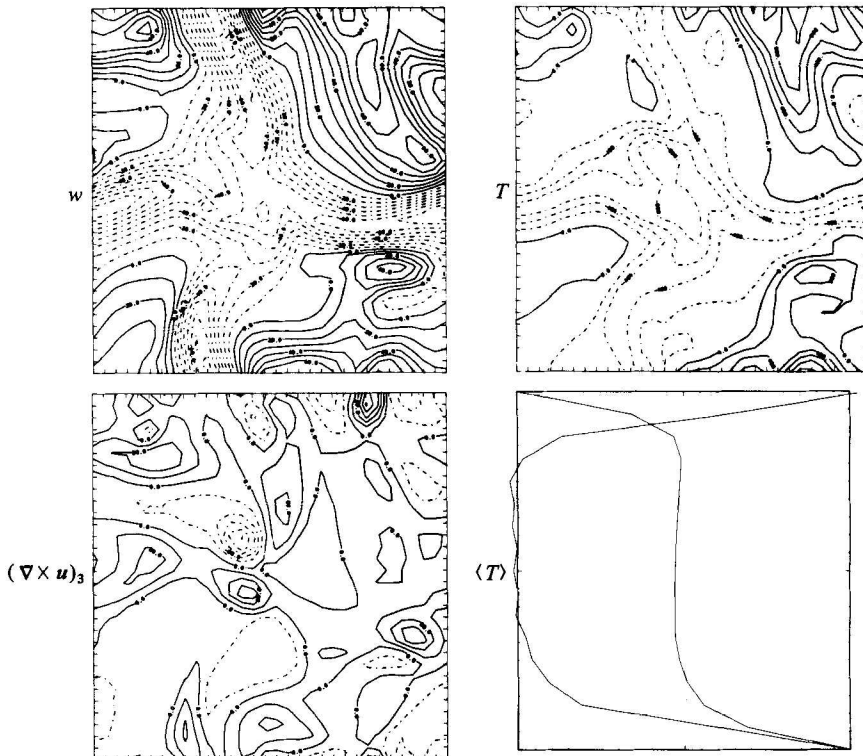
FIGURE 24. Midplane contours of (a) $w(x, y, 0.5, t)$; (b) $T(x, y, 0.5, t)$; (c) $(\nabla \times v)_3 (x, y, 0.5, t)$; (d) $\langle T \rangle (z, t)$ and $-\partial \langle T \rangle / \partial z$; all at $t = 4$ for $\sigma = 1$. These should be compared to otherwise equivalent $\sigma = 10$ results contoured in figure 22. The resolution is $32^2 \times 16$.

negative burst of relatively low frequency. This corresponds to a sweeping of the low-temperature core of the sinuous roll past the probe. This occurs somewhat arrhythmically, and the roll boundaries are somewhat ill-defined; the roll boundaries are also beginning to disintegrate, as illustrated in figure 23. In this figure we show a time series illustrating the oscillation of roll boundaries, which gives rise to an outbreak of a three-dimensional event.

Overall we note that the temperature field is considerably more turbulent than the velocity field. The reason is clearly the large Prandtl number ($\sigma = 10$). This behaviour of T is not at all unexpected. However, it suggests that more attention should be focused on temperature measurements, as opposed to velocity measurements, particularly for large-Prandtl-number fluids. If only velocity-field information were available, we would considerably under-estimate the level of turbulent activity.

5.4. *Comparison with three-dimensional results at $\sigma = 1$*

The three-dimensional flows so far described have developed a random character at large Ra, but are still strongly two-dimensional, and show only a small kinetic-energy transfer to small scales. This aspect of the flow is likely attributable to the large Prandtl number, which leads to the fact that the turbulence is more nearly an aspect of the temperature than the velocity field. This is an inhospitable regime for direct numerical calculations, because of the wide range of scales of the velocity and temperature fields. Here we present some results at $\sigma = 1$, in which the two scales are more nearly equal. The resulting flow is more nearly isotropic, and the energy transfer to small scales is larger.
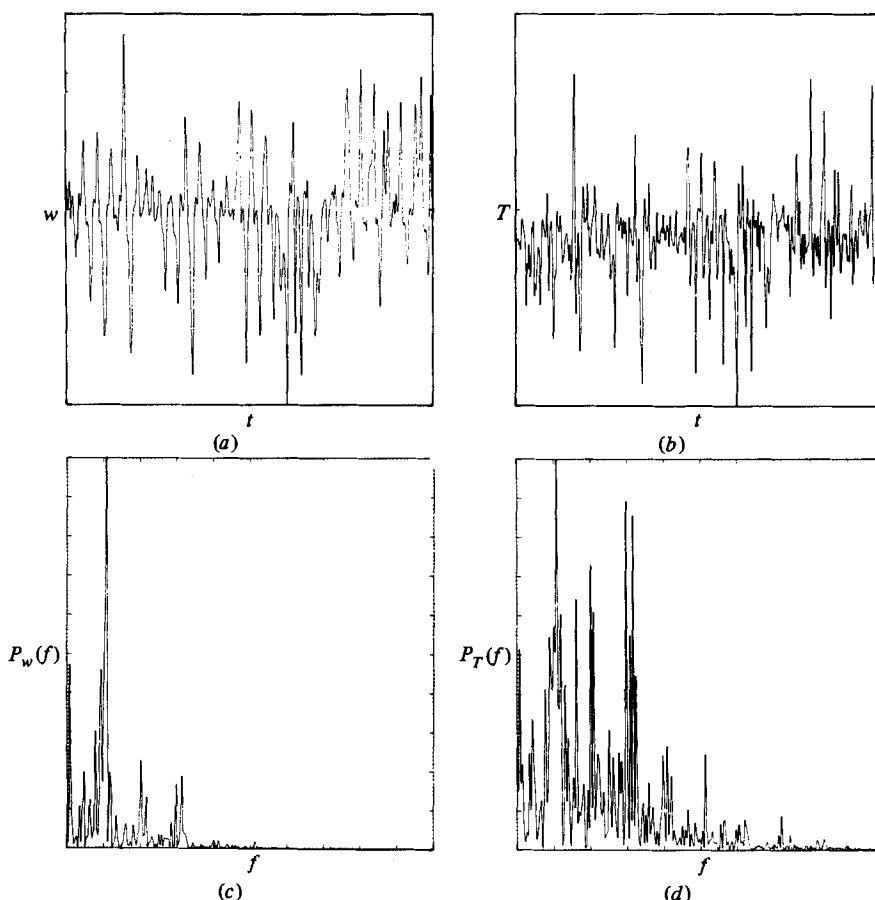
FIGURE 25. Time series of T (a) and w (b) at the midpoint of the box, and power spectral densities of T (c) and w (d) for the run 50(16³) with $\sigma = 10$ and Rayleigh-number modulaton according to (5.19) with $\epsilon = 0.1, f = 24$.

In figure 24 contour plots of w, T, $(\nabla \times \boldsymbol{u})_3$ and $\langle T \rangle (x, t)$ are given at $t = 4$ for $\sigma = 1$ for resolution $32^2 \times 16$. The same seed random number has been used as for the $\sigma = 10$ calculations shown in figure 22. A rather striking difference in the contour plots is that they now appear to be nearly statistically symmetric in (x, y). There no longer appears to be a persistent stable thermal core (although ephemeral stable gradients do appear occasionally) and, consequently, the flow is not characterized by a single oscillation at the Brunt–Väisälä frequency. The values of $S_{uuu} \approx 0.44$, $S_{uTT} \approx 0.55$, $I \approx 0.58$ and $R_\lambda \approx 14.4$ for the $Ra = 70Ra_c$, $\sigma = 1$ run are shown in figure 20 as solid circles. All of these turbulence measures (except S_{uTT}) show a marked increase above their $\sigma = 10$ values.

It is possible that the present results overestimate considerably the Rayleigh numbers at which transition to chaotic behaviour occurs.† It has been shown (Zippelius & Siggia 1982; Siggia & Zippelius 1981) that, for small σ, large-aspect-ratio convecting layers between free-slip boundaries may be unstable to modes that produce a weakly chaotic system of shifting roll patterns. We have not been able to study this possiblity with our present numerical codes.

† *Note added in proof*: For example, in some more recent studies with $\sigma = 10$ and aspect ratio $4\sqrt{2}$, transition to a weak temporal chaos is observed as low as $Ra/Ra_c \approx 3$–4.

5.5. *Effects of Rayleigh-number oscillations*

Gollub & Benson (1980) found that frequency modulation of wall temperature of the form

$$Ra(t) = Ra(0)\,[1 + \epsilon \sin 2\pi ft] \qquad (5.17)$$

induces chaotic behaviour in a quasi-periodic flow close to transition. We have investigated this phenomenon numerically in both two and three dimensions. We choose $\epsilon = 0.1$ and the oscillation frequency f to be incommensurate with the frequencies of the quasi-periodic motion.

In two dimensions we found little effect of this Rayleigh-number modulation, but in three dimensions the effect is quite striking. With 16^3 resolution, $Ra(0) = 50Ra_c$, $\epsilon = 0.1$ and $f = 24$ (between the two largest lines of the power spectrum – see figure 13) the results plotted in figure 25 are obtained. Notice the enhanced noisiness of this flow compared with that with $\epsilon = 0$ (see figures 12 and 13). This flow is even noisier than the constant-Rayleigh-number flow at $Ra = 65Ra_c$ even though $\max_t Ra(t) = 55Ra_c$. This enhanced randomness is reflected in the isotropy ratio I and skewness factor S_{uuu}. When ϵ increases from 0 to 0.1, I increases from about 0.15 to about 0.4, while S_{uuu} increases from about 0.04 to about 0.3.

These three-dimensional results support the conjecture that periodic modulation of the Rayleigh number in a two-frequency flow may provide the third frequency necessary to induce chaos in the Ruelle *et al.* scenario. However, the lack of strong chaos in the modulated two-dimensional convection problem may suggest a somewhat more subtle dynamical process.

Finally we comment on a fundamental fact found in recent experimental work of Ahlers & Behringer (1978), Gollub, McCarriar & Steinman (1982), Gollub & Benson (1980), viz that in Rayleigh–Bénard convection there is no single favoured bifurcation sequence leading to turbulence. Indeed the transition to turbulence depends on geometry and stress parameters (Ra, σ) as well as initial conditions.

Once the geometry is chosen and the parameter set is fixed, the phase space of an experiment or numerical simulation probably contains a variety of attracting solutions, either stationary, periodic or strange. Kirchartz *et al.* (1981) and Gollub *et al.* (1982) have shown that for circular and rectangular geometries multiple stable states exist just above the convective threshold in Rayleigh–Bénard convection (see also Cross *et al.* 1983). It is reasonable to expect that such solutions will become unstable as parameters are varied, and each could lead to its own distinct route to turbulence.

The three-dimensional simulations presented here are limited to box geometries with free-slip boundary conditions, so it is difficult to compare our numerical results with physical experiments. However, we have observed only one route to turbulence that parallels route I of Gollub & Benson (1980) and is consistent with the Ruelle–Takens–Newhouse (1978) scenario.

REFERENCES

BRACHET, M. E., MEIRON, D. I., ORSZAG, S. A., NICKEL, B. G., MORF, R. H. & FRISCH, U. 1983 Small-scale structure of the Taylor–Green vortex. *J. Fluid Mech.* **130**, 411–452.

BUSSE, F. H. 1972 Oscillatory instability of convection rolls in a low Prandtl number fluid. *J. Fluid Mech.* **52**, 97–112.

CROSS, M. C., DANIELS, P. G., HOHENBERG, P. C. & SIGGIA, E. D. 1983 Phase-winding solutions in a finite container above the convective threshold. *J. Fluid Mech.* **30**, 465.

CURRY, J. H. 1978 Generalized Lorenz systems. *Commun. Math. Phys.* **60**, 193–204.

CURRY, J. H. 1979 Chaotic response to periodic modulation. *Phys. Rev. Lett.* **43**, 1013–1016.

EIDSON, T. M. 1982 Numerical simulation of a turbulent Rayleigh–Bénard problem using subgrid scale modelling. Ph.D. thesis, Dept Mech. Engng, Univ. Michigan, Ann Arbor.

FEIGENBAUM, M. J. 1978 Quantitative universality for a class of nonlinear transformation. *J. Stat. Phys.* **19**, 25–52.

GOLLUB, J. P. & BENSON, S. V. 1980 Many routes to turbulent convection. *J. Fluid Mech.* **100**, 449–470.

GOLLUB, J. P., McCARRIAR, A. R. & STEINMAN, J. F. 1982 Convective pattern evolution and secondary instabilities. *J. Fluid Mech.* **125**, 259–281.

GRÖTZBACH, G. 1982 Direct numerical simulation of laminar and turbulent Bénard convection. *J. Fluid Mech.* **119**, 27–53.

GRÖTZBACH, G. 1983 Spatial resolution requirement for direct numerical simulation of Rayleigh–Bénard convection. *J. Comp. Phys.* **49**, 241–264.

HERRING, J. R. & KERR, R. M. 1982 Comparison of direct numerical simulation with predictions of two-point closures for isotropic turbulence convecting a passive scalar. *J. Fluid Mech.* **118**, 205–219.

KIRCHARTZ, K. K., MULLER, U., OERTEL, H. & ZIEREP, J. 1981 Axisymmetric and non-axisymmetric convection in a cylindrical container. *Acta Mech.* **40**, 181–194.

KRAICHNAN, R. H. 1967 Inertial ranges in two dimensional turbulence. *Phys. Fluids* **13**, 569–575.

LANDAU, L. D. & LIFSHITZ, E. M. 1959 *Fluid Mechanics.* Addison-Wesley.

LEITH, C. E. & KRAICHNAN, R. H. 1972 Predictability of turbulent flows. *J. Atmos. Sci.* **29**, 1041–1058.

LORENZ, E. N. 1963 Deterministic non-periodic flow. *J. Atmos. Sci.* **20**, 130–141.

MARCUS, P. S. 1981 Effects of truncation in modal representations of thermal convection. *J. Fluid Mech.* **103**, 241–255.

McLAUGHLIN, J. & ORSZAG, S. A. 1982 Transition from periodic to chaotic thermal convection. *J. Fluid Mech.* **122**, 123–142.

MONIN, A. S. & YAGLOM, A. M. 1975 *Statistical Fluid Mechanics*, vol. 2. MIT Press.

MOORE, D. R., TOOMRE, J., KNOBLOCH, E. & WEISS, N. O. 1983 Period doubling and chaos in partial differential equations for thermosolutal convection. *Nature* **303**, 663–667.

MOORE, D. R. & WEISS, N. O. 1973 Two-dimensional Rayleigh–Bénard convection. *J. Fluid Mech.* **58**, 289–312.

ORSZAG, S. A. 1971 Numerical simulation of incompressible flows within simple boundaries, I. Galerkin (spectral) representations. *Stud. Appl. Maths* **50**, 293–327.

ORSZAG, S. A. & KELLS, L. C. 1980 Transition to turbulence in plane Poiseuille and plane Couette flow. *J. Fluid Mech.* **96**, 159–205.

ORSZAG, S. A. & PATTERSON, G. S. 1972 Numerical simulation of turbulence. In *Statistical Models and Turbulence* (ed. M. Rosenblatt & C. Van Atta). Lecture Notes in Physics, vol. 12, pp. 127–147. Springer.

POMEAU, Y. & MANNEVILLE, P. 1980 Intermittent transition to turbulence in dissipative systems. *Commun. Math. Phys.* **74**, 189–197.

RAND, D., OSTLUND, S., SETHNA, J. & SIGGIA, E. 1982 Universal transition from quasi-periodicity to chaos in dissipative systems. *Phys. Rev. Lett.* **49**, 132–135.

ROTTA, J. C. 1951 Statistische Theorie nichthomogener Turbulenz. *Z. Phys.* **129**, 547–572.

RUELLE, D., TAKENS, F. & NEWHOUSE, S. E. 1978 Occurrence of strange axiom A attractors near quasi periodic flows on T^m, $m \geqslant 3$. *Commun. Math. Phys.* **64**, 35–40.

SCHUMANN, U. & HERRING, J. R. 1976 Axisymmetric homogeneous turbulence: a comparison of direct spectral simulations with the direct interaction approximation. *J. Fluid Mech.* **76**, 755–782.

SIGGIA, E. D. & ZIPPELIUS, A. 1981 Dynamics of defects in Rayleigh–Bénard convection. *Phys. Rev.* **A24**, 1036–1049.

TAVOULARIS, S., BENNETT, J. C. & CORRSIN, S. 1978 Velocity derivative skewness in small Reynolds number and isotropic turbulence. *J. Fluid Mech.* **88**, 63–69.

TREVE, Y. M. & MANLEY, O. P. 1982 Energy conserving Galerkin approximations for 2-d hydrodynamic and MHD Bénard convection. *Physica* **4D**, 319–342.

ZIPPELIUS, A. & SIGGIA, E. D. 1982 Disappearance of stable convection between free-slip boundaries. *Phys. Rev.* **A26**, 1788–1790.